Macromolecules

pubs.acs.org/Macromolecules Article

Crystallinity-Independent Toughness in Renewable Poly(L-lactide) Triblock Plastics

Daniel M. Krajovic, Greg Haugstad, and Marc A. Hillmyer*

Cite This: *Macromolecules* 2024, 57, 2818−2834 Read Online

ACCESS | Metrics & More | Article Recommendations | Supporting Information

ABSTRACT: Poly(L-lactide) (PLLA)'s broad applicability is hindered by its brittleness and slow crystallization kinetics. Among the strategies for developing tough, thermally resilient PLLA-based materials, the utilization of neat PLLA block polymers has received comparatively little attention, despite its attractive technological merits. In this work, we comprehensively describe the microstructural, thermal, and mechanical properties of two compositional libraries of PLLA-rich PLLA-*b*-poly(γ-methyl-ε-caprolactone) (PγMCL)-*b*-PLLA ("LML") triblock copolymers. Rubbery PγMCL domains microphase separate from the matrix in the melt and intercalate between PLLA crystal lamellae on cooling. Despite the mobility constraints associated with midblock tethering, the PLLA end-blocks crystallize as rapidly as a PLLA homopolymer control of similar molar mass. Independent of their degree of crystallinity, LML triblocks exhibit vastly improved tensile toughnesses (63−113 MJ m^{-3}) over that of PLLA homopolymer (1.3−2 MJ m^{-3}), with crystallinities of up to 55% and heat distortion temperatures (HDTs) as high as 148 °C. We investigated the microstructural origins of this appealing performance using X-ray scattering and microscopy. In the case of a largely amorphous PLLA matrix, the PγMCL domains cavitate to enable concurrent PLLA shear yielding and strain-induced crystallization. In highly crystalline PLLA matrices, PγMCL facilitates a lamellar-to-fibrillar transition during tensile deformation, the first such transition reported for PLLA drawn at room temperature. These results highlight the unique attributes of PLLA block polymers and prompt future architectural and processing optimizations to achieve ultratough, high-HDT PLLA block polymer plastics after a simple thermal history on economical time scales.

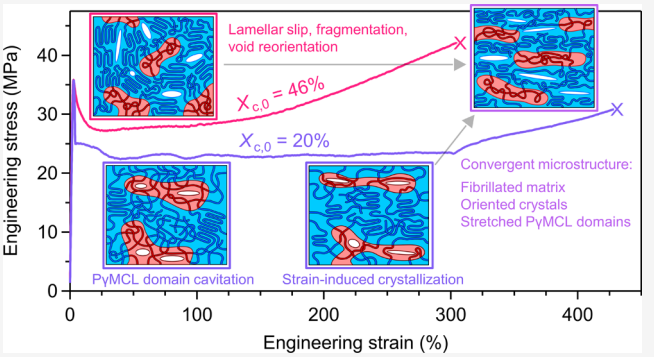

INTRODUCTION

The unique technological superiorities of plastics made them a cornerstone of the world economy, but the current paradigms of plastics manufacturing, use, and disposal pose severe ongoing harm to the biosphere.[1] Virtually all commercial plastics are fossil fuel-derived, and high rates of waste[2] and low rates of recycling[3,4] have produced an unsustainable, linear plastics life cycle. Waste mismanagement has led to widespread accumulation of plastics in terrestrial and marine ecosystems, with severe economic, public health, and infrastructural consequences.[5−7] Recent reports indicate that the already poor recycling rates have been overestimated, calling for sweeping challenges to the single-use plastic convention.[8,9] The development of renewably sourced and compostable materials with competitive properties must contribute to the continued fulfillment of plastic demand.[4]

Poly(L-lactide) (PLLA) is a promising candidate to replace oil-derived plastics. Its monomer, lactide, can be renewably produced from corn-derived dextrose,[10] and it readily undergoes hydrolytic degradation in industrial composting, enabling a circular life cycle.[11,12] PLLA homopolymer has attractive technological merits, including Young's modulus between 3 and 3.5 GPa, a tensile strength ranging from 60 to 70 MPa, and a wide processing window from 190 to 240 °C.[13] However, it is inherently brittle after short postprocessing aging periods, and its slow crystallization kinetics limit the heat distortion temperature (HDT) of products accessible under typical processing routines. Despite these drawbacks, the production capacity of high-molar mass poly(lactide) has steadily increased since its commercialization and is expected to double over the next 5 years.[14] Addressing its technical shortcomings thus has both well-defined economic and environmental benefits.

Efforts to simultaneously upgrade PLLA's thermal and mechanical properties have spawned a rich subfield. Melt-blending with rubbery polymers is the most well-explored approach, owing to the low cost of bulk rubber, translatability to existing melt-processing capabilities, and property tunability

Received: December 15, 2023
Revised: February 1, 2024
Accepted: February 5, 2024
Published: March 12, 2024

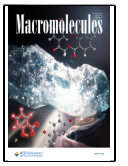

https://doi.org/10.1021/acs.macromol.3c02580
Macromolecules 2024, 57, 2818−2834

under a wide parameter space.[15,16] In blends, the most significant mechanical property enhancements most often require reactive[17−24] or nonreactive compatibilization.[25−30] In other approaches without adding rubber, polymer-grafted cellulose nanocrystals have garnered attention as crystal nucleators[31,32] and toughening.[33−35] Amphiphilic non-PLA diblock polymers have also conferred toughness and aging resistance to atactic PLA,[36−39] as well as toughness and accelerated crystallization to semicrystalline PLLA.[40,41] Finally, thermomechanical preconditioning of PLLA[42−44] and its composites[45] can produce highly oriented matrices with improved strength, ductility, and thermal resistance.

Neat PLLA block polymer plastics have received much less attention in part because their syntheses are currently less economical than blending strategies. Encouragingly, advancements in orthogonal catalysis and chemical reaction engineering are steadily expanding the arsenal of more accessible one-pot lactide ring-opening block polymerizations.[46−50] In the PLLA block polymer space, thermoplastic elastomers with PLLA-lean compositions—defined here as having a total PLLA block volume fraction (f_{PLLA}) of less than 0.5—have so far commanded much more attention than their PLLA-rich plastic counterparts ($f_{PLLA} > 0.5$).

Nonetheless, investigations into such plastic materials have yielded several key insights. Baimark and Srisuwan compared the thermal and mechanical behavior of block-miscible, PLLA-*b*-poly(ethylene glycol) (PEG)-*b*-PLLA triblocks with PEG midblock molar masses of 20 kg mol^{-1} (49-20-49 (block masses, kg mol^{-1}), f_{PLLA} = 0.81) and 35 kg mol^{-1} (47-35-47, f_{PLLA} = 0.65) with and without epoxide-mediated chain extension.[51] Despite well-entangled rubbery midblocks ($M_{e,PEG} \approx 2$ kg mol^{-1} (average molar mass between entanglements), $M_{c,PEG} \approx 5.9$ kg mol^{-1} (critical entanglement molar mass)),[52] chain extension of the triblocks into linear multiblocks was required for meaningful toughness enhancement. Lebarbé et al. investigated the thermomechanical and microstructural properties of a series of PLLA-*b*-poly(ricinoleic acid)-*b*-PLLA triblocks with $0.33 < f_{PLLA} < 0.88$.[53] The rubbery poly(ricinoleic acid) midblock molar mass was fixed at 11 kg/mol, leading to a state of poor-to-moderate entanglement (M_e = 6.2−8.1 kg mol^{-1}, assuming ρ = 1 g cm^{-3}).[54] In tensile testing, the strength and ductility both increased monotonically with increasing PLLA end-block molar mass, indicating that the properties were limited by the number of PLLA matrix entanglements.[55,56] Panthani and Bates synthesized a PLLA-*b*-poly(ethylene-*co*-ethylethylene)-*b*-PLLA ("LEL") triblock with block masses of 4.2-2.1-4.2 kg mol^{-1} (f_{PLLA} = 0.7).[57] They also chain-extended the LEL to form a linear multiblock and investigated the properties of various triblock-multiblock blends. The LEL triblock demonstrated the fastest crystallization but was highly brittle, likely due to a poor state of entanglement in both the midblock and end-blocks.[55,56,58] In contrast, the pure multiblock and multiblock-rich blends showed dramatic ductility enhancement but completely arrested PLLA crystallization. Thermally annealing the pure multiblock and a 60 wt % multiblock blend caused significant and dose-dependent reductions in ductility with increased PLLA crystallinity, which was ascribed to the consumption of matrix-bridging PLLA chains by crystals. A similar trade-off between crystallization rate and enhanced ductility was reported for chain-extended PLLA-*b*-poly(isobutylene)-*b*-PLLA triblocks with $0.061 < f_{PLLA} < 0.74$[59] and poly(ε-caprolactone)-*b*-PLLA-*b*-poly(D,L-lactide) multiblocks with f_{PLLA} = 0.8.[60] Beyond linear architectures, graft-block copolymers ($0.5 < f_{PLLA} < 0.7$) with crystallizable PLLA outer graft blocks have demonstrated substantial toughness enhancement, though at the expense of Young's modulus and with maximum crystallinities of 11%.[61,62] We desired to synthesize a PLLA block polymer with well-entangled rubbery blocks that microphase separate from an entangled PLLA matrix that can crystallize on meaningful processing time scales, producing a tough and highly crystalline plastic with a single, simple thermal history.

Poly(γ-methyl-ε-caprolactone) (PγMCL) is an appealing option for the rubbery block. Its monomer, γMCL, can be economically sourced from *p*-cresol, one of the most readily derivable components in lignin.[63] Among the alkyl-substituted lactones, γMCL is distinguished by rapid ring-opening kinetics and high equilibrium conversions due to its ring size and methyl group positioning.[64,65] PγMCL is an amorphous material with a T_g of −61 °C and a low M_e of 2.9 kg/mol, which enables a state of dense entanglement even at modest molar masses.[66] It undergoes rapid and complete hydrolysis to 6-hydroxy-4-methylhexanoic acid, which is fully mineralizable into the soil, a key compostability requirement.[67,68] As a homopolymer, PγMCL has shown excellent elastomeric performance in cross-linked,[68] covalent adaptable networks,[69,70] and hydrogen-bonding bottlebrush molecular topologies.[71] Reisman et al. verified the compostability of block polymers of PLLA and PγMCL.[72] With $f_{PLLA} < 0.5$, these block polymers microphase separate into entangled PγMCL matrices and physically cross-linked PLLA domains, producing thermally resilient, high-performing thermoplastic elastomers in linear,[66,73] star-block,[74,75] graft-block,[76] and miktoarm star architectures.[77] Efforts to translate these findings into the tough plastics space have so far been restricted to atactic, amorphous poly(lactide),[78] so the capability of PγMCL to simultaneously toughen and improve the thermal resilience of semicrystalline PLLA plastics remains uninvestigated.

Here, we produced compositionally inverted ($f_{PLLA} > 0.5$) PLLA-*b*-PγMCL-*b*-PLLA ("LML") libraries of PLLA-rich triblock polymer plastics. As part of our study, we developed two complementary methods to quantify impurity species resulting from adventitious initiation during synthesis, enabling a detailed specification of the composition of each material. The thermal properties, including dynamic and isothermal crystallization behavior along with HDTs, were measured and benchmarked against a PLLA homopolymer control. Mechanical properties were surveyed through uniaxial tensile testing of melt-pressed LML films and Izod impact testing of a scaled batch of triblock. We performed extensive X-ray scattering and microscopy experiments to characterize the pristine microstructure resulting from various processing histories, as well as *in* and *ex situ* analysis of the tensile fracture process to elucidate stress-induced microstructural changes. Using these observations, we propose mechanisms for the emergent thermal and mechanical advantages of neat LML triblock plastics.

RESULTS AND DISCUSSION

Molecular Characterization. LML triblocks were synthesized according to the protocol developed by Watts et al., as summarized in Scheme 1 below.[66] 1,4-Benzenedimethanol was used as the initiator for the homopolymerization of γMCL to form a difunctional α,ω-dihydroxy-telechelic PγMCL midblock, which was then chain-extended with L-lactide. While previous work from our group has shown that LMLs can be

https://doi.org/10.1021/acs.macromol.3c02580
Macromolecules 2024, 57, 2818−2834

Scheme 1. Synthesis of Dihydroxy-Telechelic PγMCL Macroinitiator and LML Triblocks

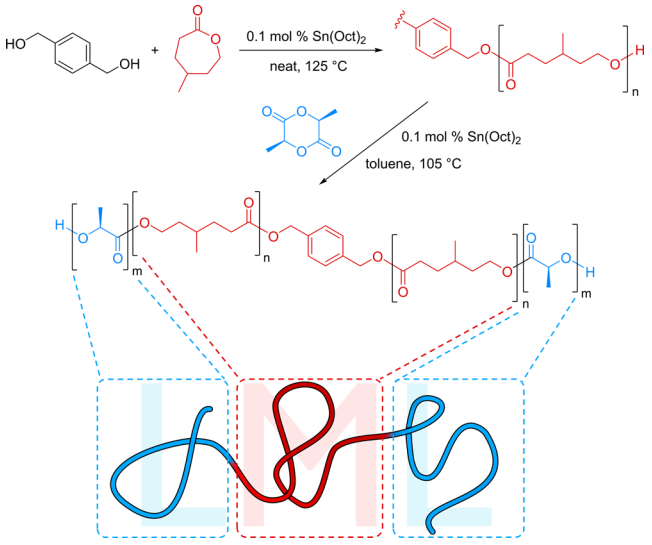

synthesized in one pot using orthogonal catalysis and minute quantities of solvent,[79] here we sought to control the polymerization conditions to keep molar mass dispersity low and ensure that our nominal f_{PLLA} descriptors were as accurate as possible. As such, we purified the PγMCL macroinitiators before chain extension in toluene. Both steps employed typical $Sn(Oct)_2$ catalysis. The naming convention for the triblocks is "LML A-B-A," where A and B are the molar masses of end- and midblocks in kg mol^{-1}. PγMCL macroinitiators are denoted as "M#", where # is the molar mass in kg mol^{-1} As a control for thermal and mechanical property studies, a 78-kg mol^{-1} linear PLLA homopolymer was synthesized with 1,4-benzenedimethanol as initiator. This homopolymer is denoted as "L78." The molar mass, dispersity, composition, and purity characteristics of the PγMCL midblocks and LML triblocks synthesized for this study are listed in Table 1.

Figures S1, S2, and S3, respectively, display the ^{1}H NMR spectra of the highly pure γMCL, L-lactide, and BDM used for synthesis. Accordingly, the spectra acquired for the PγMCL homopolymer, LML triblock, and PLLA homopolymer control (Figures S4, S5, and S6, respectively) show resonances consistent with previous reports, indicating reaction completion and negligible incidence of side reactions.[66] Furthermore, Figure S7 shows that the LML triblocks' ^{13}C NMR spectra contain only the two carbonyl resonances corresponding to the ester units in the PγMCL and PLLA homopolymers, showing no appreciable mixing of monomer repeat units.

Size exclusion chromatograms for the PγMCL midblocks and corresponding triblock libraries are displayed in Figure 1. The product traces are shifted to lower retention volumes than the PγMCL midblock trace after chain extension as expected. Low-molar mass shoulders or secondary peaks appear in all the triblock traces, indicative of some unreacted PγMCL macroinitiator, "LM" diblocks resulting from monofunctional impurity PγMCL chains, macrocyclic PLLA produced from backbiting reactions, or linear homopolymer PLLA initiated by adventitious impurities. The α-hydroxy methylene protons at the ends of the PγMCL macroinitiator, which appear initially in ^{1}H NMR spectra as a multiplet spanning δ = 3.77−3.61 ppm, are absent in all LML triblock spectra, supporting the reaction of all macroinitiators (Figure S8). However, in this

Table 1. Molecular Characteristics of PLLA Control, PγMCL Mid-Blocks, and LML Triblocks

designation	$M_{n,\,P\gamma MCL}$ (kg mol^{-1})[a]	$M_{n,\,PLLA,\,arm}$ (kg mol^{-1})[a]	$M_{n,\,LML,\,tot}$ (kg mol^{-1})[a]	$M_{w,\,SEC\,MALLS}$ (kg mol^{-1})[b]	$Đ_{SEC\,RI}$[c]	$f_{PLLA,\,tot}$[d]	w_{LML}[e]	w_{LM}[e]	w_{hPLLA}[e]
L78	—	77.8	—	54.1	1.1	1.0	0.98	0	0.020[f]
M11	11.3	—	—	13.4	1.4	—	—	—	—
LML 11-11-11	11.3	11.0	33.4	29.5	1.2	0.64	0.92	0.019	0.058
LML 24-11-24	11.3	24.5	60.3	54.1	1.2	0.80	0.89	0.056	0.052
LML 63-11-63	11.3	63.1	126	121	1.1	0.91	0.82	0.026	0.15
M22	22.1	—	—	26.5	1.2	—	—	—	—
LML 18-22-18	22.1	17.8	57.6	55.0	1.2	0.61	0.87	0.019	0.11
LML 37-22-37	22.1	36.7	95.5	82.1	1.2	0.77	0.77	0.025	0.21
LML 43-22-43	22.1	42.7	108	100	1.2	0.78	0.95	0.016	0.038
LML 137-22-137	22.1	137	295	280	1.1	0.92	0.58	0.10	0.32

[a]Determined using ^{1}H NMR spectroscopy end-group analysis. [b]Determined using $CHCl_3$−SEC multiangle laser light scattering (MALLS) detection. [c]Determined using $CHCl_3$−SEC differential refractive index (RI) detection. [d]Total PLLA volume fraction, accounting for impurity species, calculated from block M_n values using $\rho_{P\gamma MCL}$ = 1.037 g cm^{-3} and ρ_{PLLA} = 1.25 g cm^{-3}.[10,66] [e]Weight fractions of impurity diblock ("LM") and PLLA homopolymer ("hPLLA"); calculated from SEC traces (Scheme S13). [f]PLLA homopolymer impurity in the homopolymer control refers to species that have half the molar mass of the targeted chains due to initiation by monofunctional impurities as opposed to BDM. This was calculated by comparing BDM midgroup and PγMCL methyl ester resonances to PLLA end-group resonances in ^{1}H NMR spectroscopy (Scheme S9)

https://doi.org/10.1021/acs.macromol.3c02580
Macromolecules 2024, 57, 2818−2834

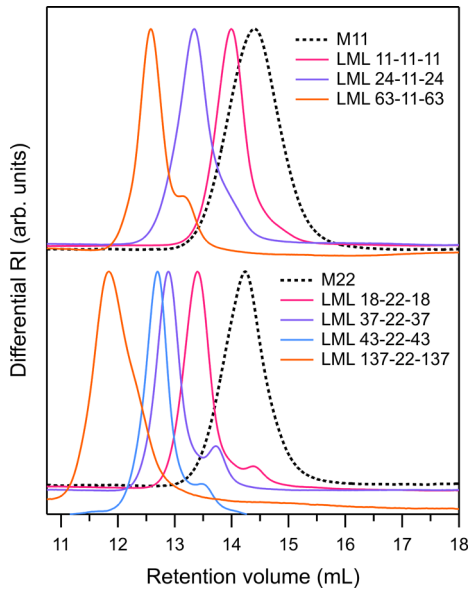

Figure 1. Differential refractive index chromatograms for M11 and the resulting 11-kg mol^{-1} midblock LML library (top) and for M22 and the resulting 22-kg mol^{-1} midblock LML library (bottom). Traces are normalized such that the maximum signal value in the analytical retention volume range is set to unity.

region, a singlet is visible at 3.66 ppm, consistent with methanol-initiated, monofunctional PγMCL,[79] suggesting that LM diblocks were produced. We also measured an excess of PLLA end-group methine protons with respect to the PγMCL midgroup aryl protons relative to the ideal case of a pure triblock. Reasoning that the major impurity species must have contributed additional end-groups, we assumed a negligible abundance of macrocyclic species. Using the relative integrations of PγMCL methyl ester, PLLA end-group methine, and PγMCL midgroup aryl proton resonances, we calculated the mole fractions of "LM" diblock and linear PLLA homopolymer impurity as described in the Supporting Information (Scheme S9). In Scheme S10, we show that this procedure can be generalized to any *f*-armed star-block polymers (including diblocks and triblocks, corresponding to f = 1 and 2, respectively) synthesized through the chain extension of a telechelic macroinitiator.

The weight fraction of impurities is more relevant to material properties than the mole fraction, and its calculation requires an estimate of the impurity species' molar masses. It is generally accepted that L-lactide polymerization with $Sn(Oct)_2$ catalyst behaves in a controlled manner, with the rate of initiation far exceeding that of propagation, M_n linearly proportional to conversion, and reaction kinetics well-described by a pseudo-first-order model.[80,81] If there is no difference in the rate constants of initiation by monofunctional impurities (e.g., water, lactic acid, lactoyllactic acid, and methanol) and the telechelic PγMCL chain ends, then on average, the molar masses of the PLLA homopolymer impurities and the PLLA blocks of LM and LML molecules would be equivalent. We verified this assumption for our system through a trial chain extension reaction. The mole fraction of impurity chains was constant throughout the polymerization, and the M_n values for the impurity distribution matched the PLLA end-block size calculated from the LML distribution in SEC (Figure S11). We then calculated impurity weight fractions from the assumption of PLLA block size equivalence (Table S12). The above scheme has a key limitation, however: it uses relative integrations of mid- and end-group ^{1}H NMR resonances, which become increasingly inaccurate with increasing molar mass due to signal-to-noise limitations. As such, we devised a method for extracting impurity species weight fractions directly from the differential refractive index (dRI) SEC traces after peak deconvolution and

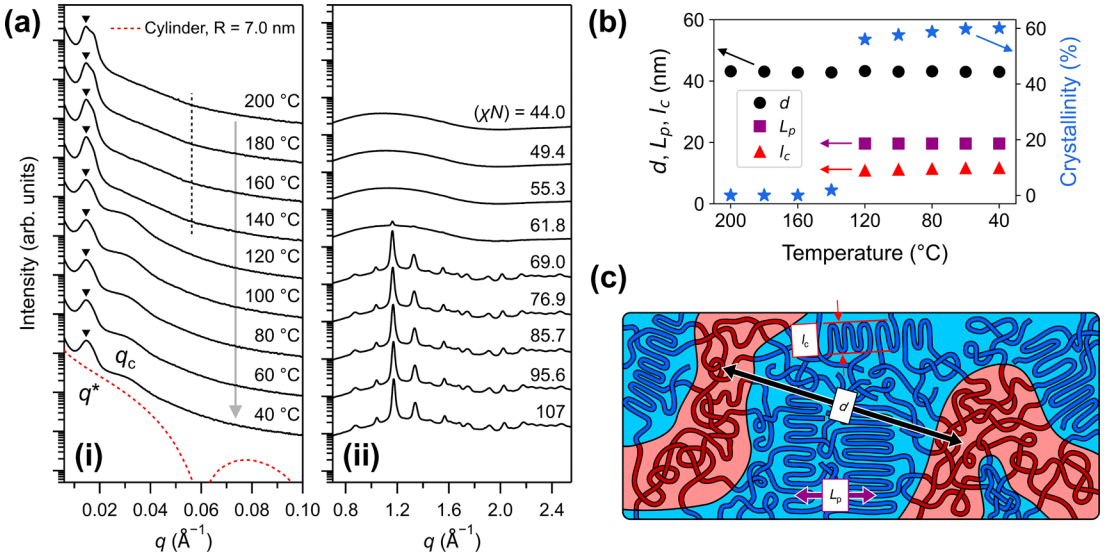

Figure 2. (a) One-dimensional (i) SAXS and (ii) WAXS patterns obtained from full azimuthal integration of 2D scattering images collected during staged cooling of LML 37-22-37 from the melt. The sample had been annealed at 200 °C for 77 min prior to the first pattern collection, and it was annealed for 5 min at each temperature before pattern collection. The principal correlation peak in the SAXS patterns is marked with an inverted black triangle. The dashed vertical line is aligned with the first extinction of the simulated cylindrical form factor (see discussion below) as a visual guide. (b) Plot of PγMCL domain spacing (d), PLLA crystal lamellar long period (L_p), lamellar thickness (l_c), and crystallinity calculated from the patterns in (a). (c) Cartoon schematic of the highly crystalline LML microstructure. Red chains are PγMCL, and blue chains are PLLA. Relative length scales are represented as accurately as possible.

https://doi.org/10.1021/acs.macromol.3c02580
Macromolecules 2024, 57, 2818−2834

accounting for the different (dn/dc) values among the blocks (Scheme S13, Figure S14, and Table S15).

For LML 11-11-11 and 18-22-18, there is excellent agreement between the two methods; the weight fractions calculated for all species are within one percent of each other. Additionally, the SEC analysis affirms that the PLLA homopolymer outweighs the LM diblock, except for LML 24-11-24, for which they are roughly equal in weight fraction. For fixed impurity concentration in the L-lactide feedstock, the weight fraction of triblock would be expected to fall with increasing f_{PLLA}. The SEC method reveals this trend, while the ^{1}H NMR method does not. This discrepancy reflects the decreasing accuracy of the relative integrals and is underscored by the fact that the discrepancies are larger for the 22-kg mol^{-1} midblock library. Despite the extensive measures taken to reduce the incidence of impurity initiation, with L-lactide recrystallized six times and the PγMCL predried in a stock solution, the triblock weight fractions calculated from SEC for LML 37-22-37 (77%) and LML 137-22-137 (58%) were 7 and 30% lower than the estimates from the ^{1}H NMR method, respectively. Encouragingly, switching to fully inert recrystallization using cannulation techniques increased the triblock weight fraction from 77 to 95% when comparing LML 37-22-37 and LML 43-22-43, for which the targeted f_{PLLA} was the same. These results highlight the sensitivity of lactide chain-extension reactions to impurity content and motivate more rigorous impurity quantification beyond the typical qualitative analysis of SEC trace modalities. The complementary quantification methods developed in this work can be used to calculate reasonable bounds for impurity contents and identify modifications to synthetic procedures that meaningfully reduce the incidence of adventitious impurity initiation.

Pristine Microstructure. To evaluate the competition between microphase separation and end-block crystallization in the LML triblocks, we collected small-angle (SAXS) and wide-angle X-ray scattering (WAXS) patterns during an extended melt-annealing period and then during a subsequent staged cooling period. Figures S16 and 2a respectively show the one-dimensional patterns for LML 37-22-37 during the melt-annealing and cooling stages, with the listed collection temperatures and associated segregation strengths (χN) calculated based on the previously determined χ(T) and using a reference volume of 118 Å^3.[66] After annealing for more than 1 h at 200 °C, only a single broad correlation peak is observed at q^* = 0.0146 Å^{-1}, indicating a disordered microphase-separated structure with an average PγMCL domain spacing of 43 nm. Uniquely out of all the LML triblocks, LML 37-22-37 exhibited two convolved correlation peaks that persisted throughout the entire melt-annealing period, suggesting a coexistence of two disordered phases with slightly different average PγMCL domain spacings. The 21 wt % PLLA homopolymer in this material may not have been uniformly solubilized in the end-block matrix, producing "dry brush" behavior and swelling some matrix regions more than others, creating a bimodal distribution of PγMCL domain spacings.[82]

The ordering behavior of the LML triblocks is strongly dependent on the total molar mass. Figures S17−S23 display the SAXS and WAXS patterns collected during melt-annealing and cooling for L78 and all other LML triblocks. LML 11-11-11, the smallest triblock, is only very weakly segregated in the melt (χN = 15.7) and then undergoes a clear disorder-to-order transition between 180 and 160 °C (χN 17.7 → 19.8) with the sudden sharpening of the principal structure factor peak, though no higher-order peaks are visible, indicating short-range order (Figure S18). In contrast, LML 24−11−24 exhibits a sharp principal peak throughout the melt-annealing period (χN = 27.5) and a weak secondary peak at $\sqrt{3}$ q^*, suggestive of a hexagonally packed cylinder (HEX) morphology (Figure S19). On initial cooling, another weak secondary peak at $\sqrt{2}$ q^* appears, corresponding to the (200) reflection of a body-centered cubic (BCC) morphology. A coexistence of these phases is plausible considering that the (f_{PLLA}, χN) coordinates in this vicinity are close to the HEX-BCC order−order transition predicted from self-consistent field theory (SCFT).[83] LML 18-22-18 displays a somewhat broad principal peak during annealing (χN = 27.3) that sharpens slightly on cooling (Figure S21). Interestingly, during a second trial of the experiment on the same LML 18-22-18 sample, multiple higher-order HEX peaks appear, and all structure factor peaks intensify over the course of the melt-annealing period (Figure S22), pointing to a kinetically limited ordering process. All LML triblocks with larger total molar masses (63-11-63, 37-22-37, and 137-22-137) display a single broad correlation peak in the melt that intensifies slightly with cooling alongside diffuse form factor scattering, indicating disordered and poorly defined PγMCL domains distributed through the PLLA matrix (Figures 2a and S16, S20, and S23). This suggests a kinetic encumbrance to ordering above a certain threshold for total molar mass, which for our system is approximately 60 kg mol^{-1}.

In all materials, crystallization of the PLLA matrix begins to proceed rapidly from 140 to 120 °C as evidenced by the stark intensification of WAXS Bragg peaks and the appearance of a broad SAXS peak corresponding to the crystal lamellar long period. For LML 11-11-11, the sharp principal structure factor peak at 140 °C is replaced by a broader, more diffuse peak centered at the same scattering vector (Figure S18c). While the relative contributions of PγMCL domain structure and crystal lamellar periodicity to this peak are uncertain, the abrupt loss of structure suggests that crystallization disrupts the melt morphology and relegates the PγMCL to the interlamellar amorphous regions.[84,85] LML 11-11-11 is most susceptible to this phenomenon due to its weak segregation at the onset of crystallization (χN = 22.1)[86] During crystallization of all the other, more strongly segregated triblocks, the correlation peak is diminished and broadened but persists separately from the lamellar spacing peak, which appears at a higher scattering vector. These features reveal that crystallization proceeds from a heterogeneous melt whose microstructure is perturbed but not destroyed and that, on average, more than one PLLA crystal lamella exists between PγMCL domains. This behavior is opposite to that observed for block polymers that undergo crystallization-induced microphase separation, in which the lamellar long period exceeds the domain spacing of the noncrystallizing block.[87]

The domain spacings, lamellar spacings, thicknesses, and crystallinities are plotted in Figure 2b for LML 37-22-37 and in Figure S24 for the other species. For LML 24-11-24 and LML 137-22-137, the PγMCL domain spacing is unchanged throughout crystallization, whereas for LML 18-22-18 and LML 63-11-63, crystallization causes a slight increase in the PγMCL domain spacing. Because the crystallization-induced densification of the matrix would, to the contrary, be expected to contract the domain spacing, a topological modification is

https://doi.org/10.1021/acs.macromol.3c02580
Macromolecules 2024, 57, 2818−2834

more likely—for instance, breaking up the PγMCL domains into smaller, more numerous disordered objects. Taking the ratio of q_c to q^* gives an estimate of the number of PLLA crystal lamellae between the PγMCL domains. This ratio ranges from ∼1 for the weakly segregated LML 11-11-11 to 2.6 for LML 63-11-63, suggesting that one to three lamellae exist between rubbery domains, on average. Figure 2c summarizes the findings from scattering in a cartoon schematic of the pristine microstructure for higher-molar-mass LMLs after matrix crystallization.

The relationship between the LML triblocks' degrees of polymerization (N_0) and the PγMCL domain spacings (d) in the melt and after staged cooling is displayed in Figure S25. N_0 was calculated following the procedure of Koo et al.; the triblock molar mass was converted to a 118 Å^3-referenced degree of polymerization and divided by two to account for the triblock architecture.[85] All LMLs except for 137-22-137 obey the mean-field scaling predicted for strongly segregated amorphous polymers, $d \sim N_0^{2/3}$, while LML 137−22−137's spacing falls below the predicted scaling. LML 137-22-137 has the highest content of impurity PLLA homopolymer determined from SEC trace deconvolution (32 wt %), which likely plays a part in this deviation. Macrophase separation of impurity homopolymers is generally expected in the limit of high homopolymer molar mass or high homopolymer content at molar masses comparable to that of the matching host block.[88] Here, it is likely that LML 137-22-137 underwent macrophase separation, with the triblock phase producing domain spacings closer to equilibrium (albeit still kinetically encumbered as discussed above), while the other triblocks were sufficiently lean in the PLLA homopolymer such that it was solubilized in the matrix, expanding the domain spacings relative to equilibrium. Figure S23a shows that during melt annealing, LML 137-22-137's correlation peak sharpens, and its form factor scattering becomes more pronounced, signaling a progressive narrowing of the distribution of PγMCL domain spacings and ripening of the domain shape, which could be occurring within the triblock phase of the two-phase melt. Meanwhile, with the same f_{PLLA} and less PLLA homopolymer impurity, LML 63-11-63 shows a static SAXS pattern throughout melt annealing, suggesting that it is instead a one-phase melt that solubilizes the homopolymer in the matrix (Figure S20a).

To examine any potential effects of ordering on crystallization, we subjected the three triblocks displaying ordered characteristics—LMLs 11-11-11, 24-11-24, and 18-22-18—to isothermal melt crystallization while monitoring microstructure with X-ray scattering using two thermal histories. In the first, we melt-annealed the samples at 200 °C (10 min), cooled them to 170 °C (30 min) to increase segregation strength while forestalling crystallization, and then cooled them to 130 °C (100 min) to induce crystallization. In the second, the samples were quenched directly from 200 (10 min) to 130 °C (100 min). The SAXS and WAXS patterns collected during these trials are shown in Figures S26−S31, from which the scattering invariant (Q) and crystallinity (X_c) were calculated as described in the Supporting Information.

As with staged cooling, the structure factor peaks observed in the melt intensify on cooling and persist separately from the lamellar spacing peak that appears during the ensuing crystallization. LMLs 11-11-11 and 18-22-18 exhibit higher-order peaks at 2 q^* and $\sqrt{7}$ q^* when cooled to 130 °C, signaling a HEX morphology. These peaks soon vanish as Bragg peaks emerge in WAXS, indicating that crystallization destroys the long-range order but preserves the principal PγMCL domain spacing observed in the melt state. Plots of Q and X_c as a function of time are shown in Figures S32a,b and S32c,d, respectively. The relative crystallization half-times are identified in Figure S32c,d as vertical lines. The 170 °C annealing period appears to accelerate subsequent crystallization at 130 °C; the half-times for LMLs 11-11-11, 24-11-24, and 18-22-18 were, respectively, reduced from 9.3 to 4.6, from 8.2 to 5.7, and from 9.2 to 4.4 min relative to the case of rapid quenching to 130 °C. Scrutinizing the invariant provides a possible acceleration mechanism. The invariant is a measure of the total scattering power and is directly proportional to the mean-square electron density fluctuation across the entire sample. Figure S32a shows that cooling from 200 to 170 °C produces an immediate, subtle increase in Q that is correlated to the extent of sharpening of the principal structure factor peak across the three LMLs. Such a rise in Q upon ordering has previously been documented for poly(isoprene)-*b*-PLA diblocks.[89] Only after 20 min of annealing, the crystallization process initiates. The PLLA crystal nuclei then speed the subsequent crystallization at 130 °C (Figure S32c). We hypothesize that the ordering that occurs during annealing at 170 °C is accompanied by interfacial sharpening that provides heterogeneous nucleation surfaces for the PLLA crystallites. *Ex situ* DSC analysis provides further support for the interfacial nucleation hypothesis as discussed in the Supporting Information (Figure S33).

To complement scattering with real-space imaging, we performed atomic force microscopy (AFM) on LML triblock film specimens after imposing various thermal histories. Figures 3a and S34 display the "tapping" (AC) mode phase images captured for LML 37-22-37 after rapid quenching from the melt to room temperature. This thermal history produces

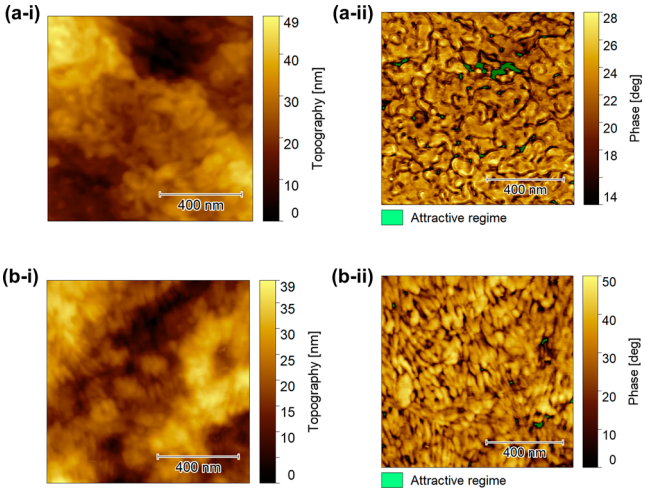

Figure 3. AFM images of pristine LML 37-22-37 films with the following thermal histories: (a) quenching rapidly from the melt to room temperature and (b) quenching rapidly to 100 °C, holding isothermally for 5 min, and quenching rapidly to room temperature. Subpanels (i) and (ii) respectively show height (plane-fit) and AC phase images. Here in the net repulsive regime (see SI), the rubbery PγMCL domains are more dissipative than the glassy PLLA matrix, and so they produce lower AC phase during tip interaction and are rendered as the darker regions of the phase images. The image size is 1 × 1 μm.

https://doi.org/10.1021/acs.macromol.3c02580
Macromolecules 2024, 57, 2818−2834

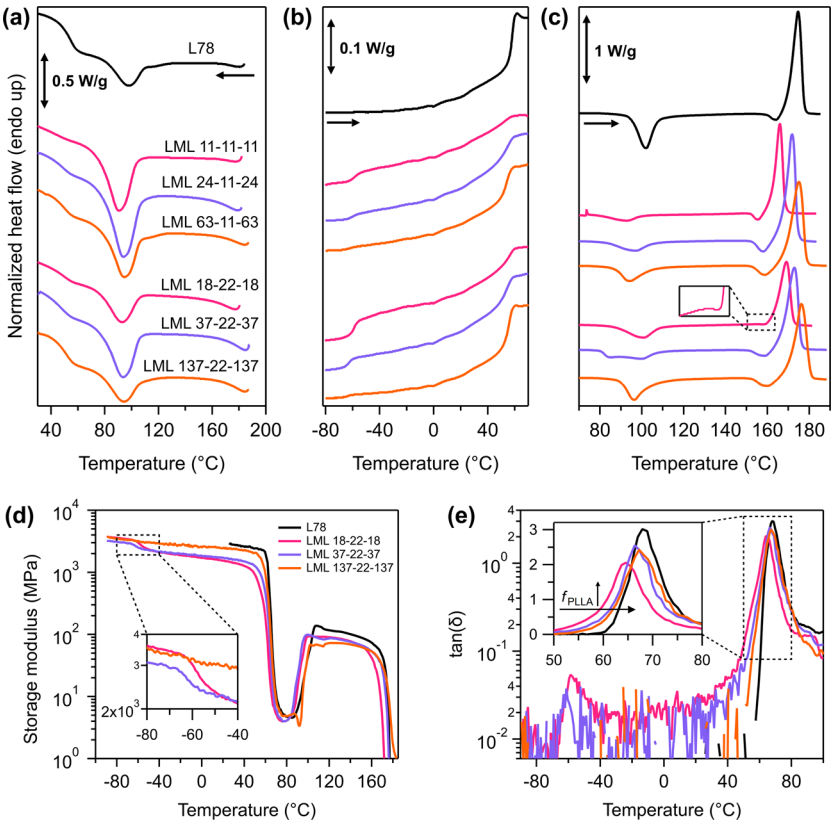

Figure 4. DSC thermograms collected during (a) first cooling after complete melting and (b) on subsequent heating at 10 °C/min. Panel (b) magnifies −80 to 70 °C, spanning the T_gs of PγMCL and PLLA, and panel (c) magnifies 70 to 190 °C, spanning cold crystallization and melting processes. The inset in panel (c) magnifies the pre-melting crystallization region for LML 18-22-18. The trace staggering and labeling scheme is consistent from (a) to (c). (d) Storage moduli and (e) loss tangents recorded during DMTA temperature sweeps for 22-kg mol^{-1} midblock LML library after rapid quenching from the melt. The insets in (d) and (e), respectively, magnify transitions associated with $T_{g,P\gamma MCL}$ and $T_{g,PLLA}$.

disordered, microphase-separated PγMCL domains dispersed throughout the matrix, consistent with conclusions from SAXS. The PγMCL appears to be part of a network of extended, wormlike domains that percolate throughout the material. Figure 3b presents the images for the same material after 5 min of melt crystallization at 100 °C. Crystal lamellae are identified as domains of higher phase (brightest/least dissipative), and the PγMCL domains (lowest phase/most dissipative) are sporadically positioned between lamellae, retaining some degree of apparent continuity. Phase images with extracted line profiles are shown in Figure S35. For melt-crystallized L78, the phase varies by at most 10° from crystalline to amorphous regions, whereas for LML 37-22-37, there are clear regions where the phase drops by 20−40 degrees, signifying a transition from the crystalline PLLA matrix to the much more dissipative PγMCL domains. In between the low-phase regions, phase variations matching those of L78's lamellar texture are observed. This corroborates the finding from scattering that $q^* < q_c$ and further supports our hypothesis of a PγMCL-templated matrix crystallization process. LML 18-22-18 behaves similarly to LML 37-22-37 (Figure S36a). In contrast, LML 137-22-137 contains discontinuous, less regularly spaced rubbery domains after both quenching and melt crystallization (Figure S38).

To conclude the discussion of pristine microstructure, it is worth noting that along with the slow melt diffusion of large LML chains, the finite weight fractions of homopolymer may influence the accessible morphologies. Blends of A-rich ABA triblock polymers and small volume fractions of "A" homopolymer exhibit disordered micelle equilibrium structures, which could suitably describe the LML microstructures and would suggest that diffusion is not rate-limiting.[90] Macrophase separation is also possible, as discussed previously, in which case the ordering of an LML-rich phase could be delayed by impurity chain exclusion. We postulate that the observed LML microstructures reflect both the thermodynamics of homopolymer PLLA solubilization and the kinetics of melt diffusion. Further work examining the influence of controlled loadings of the homopolymer is necessary to specify true equilibrium morphologies and refine the molar mass threshold for diffusion-limited ordering in true single-component LML melts.

Thermal and Thermomechanical Characterization. We performed thermogravimetric analysis (TGA) to assess the thermal stability of the LML triblocks (Figure S39). The triblocks undergo a two-stage mass loss process, with the first corresponding to PLLA degradation and the second corresponding to PγMCL degradation based on the relative areas of the temperature derivative peaks. PγMCL decomposes at a lower temperature than that of PLLA homopolymers, but this is reversed for all LML triblocks. The greater abundances of hydroxyl groups from PLLA impurity chains would lead to more frequent chain scission events.[91] A molar mass effect is apparent in LML 11-11-11 and LML 137-22-137, which respectively had the smallest (297 °C) and largest (323 °C) $T_{d,\,5\%}$ (5% mass loss temperature) values. The range of LML degradation temperatures exceeds typical processing temperatures for PLLA-based materials (e.g., 180−210 °C).

https://doi.org/10.1021/acs.macromol.3c02580
Macromolecules 2024, 57, 2818−2834

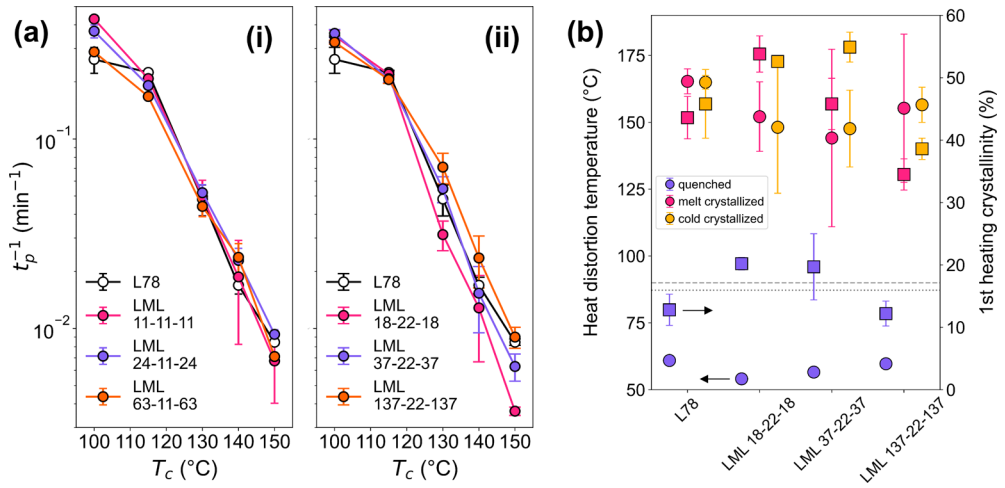

Figure 5. (a) Inverse exotherm peak times recorded during isothermal crystallization of (i) 11-kg mol^{-1} midblock and (ii) 22-kg mol^{-1} midblock LML libraries at various crystallization temperatures. The behavior of L78 is also shown for comparison. (b) HDTs and crystallinities resulting from three thermal histories imposed on L78 and the 22-kg mol^{-1} midblock LML series. All error bars denote 95% confidence intervals calculated using a student's *t*-test statistic. Deflection versus temperature traces collected in HDT testing are shown in Figure S47.

To compare the intrinsic thermal characteristics of the LML triblocks and L78, we performed differential scanning calorimetry (DSC) and dynamic mechanical thermal analysis (DMTA) (Figure 4, Table S40). After initial melting during the cooling cycle, the polymers exhibit an exotherm with peak PLLA crystallization temperatures (T_c) between 90 and 98 °C. L78 shows the highest T_c but the smallest crystallization enthalpy, signifying the most efficient PLLA crystal nucleation but the least complete crystallization process.[92] In the T_c regime of dynamic crystallization, covalent block tethering may reduce conformational freedom such that larger undercooling is required for primary nucleation. $T_{g,P\gamma MCL}$ and $T_{g,PLLA}$ are distinctly observed for all LML triblocks, corroborating the microphase-separated microstructure. The magnitude of the heat capacity increase in DSC and storage modulus decrease in DMTA at each glass transition is correlated to the abundance of the associated block (Figures 4a–d). DMTA also reveals that the loss tangent peak at $T_{g,PLLA}$ narrows and shifts to higher temperatures for LMLs containing more PLLA (Figure 4e). Because interfacial mobility coupling of glassy chains to rubbery domains is more pronounced for shorter end-blocks,[93] the LML end-block relaxation begins at the lowest temperature for LML 18-22-18 (f_{PLLA} = 0.6) and then shifts to higher temperatures as f_{PLLA} increases.

Cold crystallization of the PLLA end-blocks occurs between 80 and 105 °C upon second heating, leading to a rubbery plateau storage modulus of ∼100 MPa typical for PLLA-based materials.[94] LML 37-22-37 uniquely displays a bimodal cold crystallization exotherm, with a slightly larger primary peak with an average cold crystallization temperature (T_{cc}) of 95 °C preceded by a secondary peak or shoulder (over three replicates) at 85 °C. Because LML 37-22-37 has the largest weight fraction of impurity PLLA homopolymer out of the suspected single-phase materials (see Table 1), a partial fractionation process may occur. On second heating, the more mobile, untethered homopolymer crystallizes at a lower T_{cc}, followed by the more encumbered LML end-blocks at a higher T_{cc}. The PLLA crystal melting endotherm appears as a large peak ranging from 165 to 176 °C, with T_m correlated to the PLLA end-block or homopolymer molar mass as expected.[95] Each of these endotherms is preceded by a small premelting crystallization ("pmc" in Table S40) exotherm indicative of a polymorphic transformation of less stable α' crystallites into the more stable α form.[96] WAXS patterns acquired during staged cooling show the (004)/(103) Bragg reflection from the α-form unit cell at q = 0.88 Å^{-1} (Figure 2a).[97] In films deliberately crystallized at 100 °C for mechanical testing as described below, the (004)/(103) reflection is less prominent and is accompanied by the subtle (016)/(106) α' reflection at 1.72 Å^{-1} (Figures S55a and S63a).[97] Therefore, a coexistence of α and α' crystal polymorphs evolves from the cooling routines explored here. This is consistent with the nucleation of α-form crystals above 120 °C during cooling and their subsequent growth alongside the nucleation and growth of α'-form crystals at lower temperatures.[98]

To evaluate the rate of LML end-block crystallization, we examined isothermal melt crystallization behavior at crystallization temperatures (T_c) of 100, 115, 130, 140, and 150 °C and benchmarked them against the behavior of L78. We used the inverse of the crystallization exotherm peak time (t_p^{-1}) as a proxy for the overall speed of the crystallization process (Figure 5a).[99,100] For all polymers, the crystallization rate is largest at 100 °C and then monotonically decreases with increasing T_c. All LML triblocks except LML 63-11-63 outpace L78 crystallization at 100 °C and then more closely mirror its behavior for $T_c \geq$ 115 °C. Because LMLs with end-blocks both larger and smaller than L78 chains crystallize more rapidly than L78, we ascribe this acceleration to the triblock architecture and not to the end-block size. Polarized light optical microscopy (PLOM) reveals that LML 37-22-37 has a higher nucleation density than L78 at T_c = 100 °C, suggesting that the PγMCL domain interfaces may provide heterogeneous nucleation sites for PLLA crystallites (Figure S41a). At T_c = 130 °C, L78 and LML 37–22–37 crystallize at similar rates (Figure 5a-ii), with PLOM showing that LML 37-22-37 has a higher spherulitic growth rate and shorter nucleation induction time than L78 (Figure S41b,c). Hoffman–Weeks extrapolations[101] of apparent T_m values recorded for the various T_c conditions indicate that the equilibrium melting temperatures of all LML triblocks are depressed relative to L78 even after correction for end-block molar mass, suggesting that the PγMCL domains constrain crystal lamellar thickness (Figure

https://doi.org/10.1021/acs.macromol.3c02580
Macromolecules 2024, 57, 2818–2834

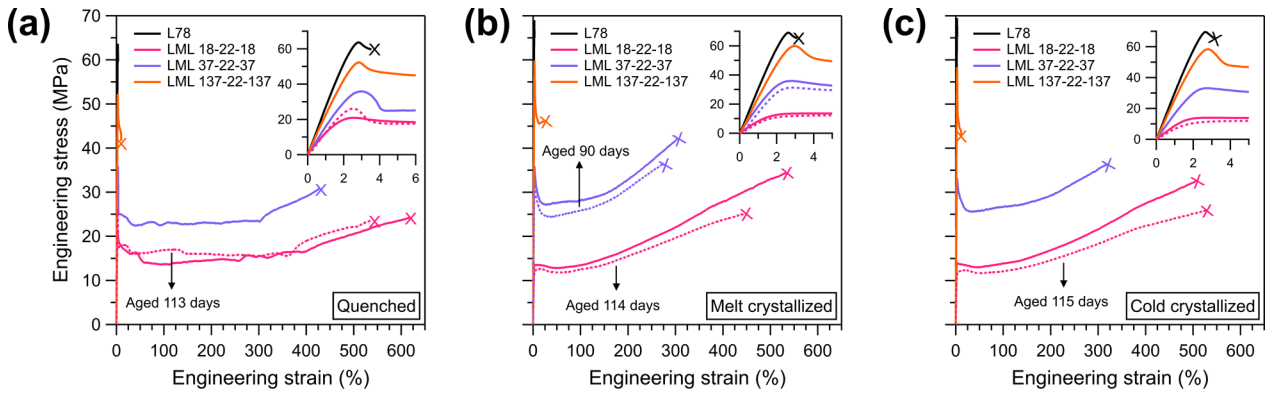

Figure 6. Representative stress−strain curves recorded during uniaxial tensile testing of dog-bone film specimens produced from three thermal histories: (a) rapidly quenching from the melt to room temperature; (b) melt crystallization at 100 °C for 5 min; and (c) cold crystallization at 100 °C for 5 min. All samples were aged at room temperature for 12 days prior to testing unless indicated otherwise.

Table 2. Summary of Thermal and Mechanical Properties of L78 Control and 22-kg mol^{-1} Midblock LML Library[a]

polymer, thermal history	X_c (%)[b]	HDT (°C)[c]	E (GPa)[d]	σ_y (MPa)	ε_B (%)	σ_B (MPa)	toughness (MJ m^{-3})
L78, q	13 ± 2	61 ± 1	3.0 ± 0.1	65 ± 1	4 ± 1	60 ± 2	2 ± 1
L78, mc	44 ± 3	165 ± 5	3.1 ± 0.1	68 ± 2	3.0 ± 0.3	64 ± 2	1.2 ± 0.2
L78, cc	46 ± 6	165 ± 3	3.1 ± 0.1	69 ± 1	3 ± 1	66 ± 3	1.3 ± 0.4
LML 18-22-18, q	20 ± 1	54 ± 0.4	1.2 ± 0.1	23 ± 1	577 ± 37	22 ± 3	94 ± 10
LML 18-22-18, mc	54 ± 3	152 ± 13	0.96 ± 0.11	14 ± 1	540 ± 33	34 ± 1	113 ± 8
LML 18-22-18, cc	53 ± 1	148 ± 25	1.00 ± 0.04	14.2 ± 0.3	494 ± 15	33 ± 1	102 ± 4
LML 37-22-37, q	20 ± 5	57 ± 2	1.8 ± 0.1	38 ± 2	297 ± 131	26 ± 3	71 ± 32
LML 37-22-37, mc	46 ± 4	144 ± 33	1.8 ± 0.2	35 ± 1	290 ± 30	39 ± 2	89 ± 10
LML 37-22-37, cc	55 ± 2	148 ± 14	1.8 ± 0.2	33 ± 1	217 ± 133	33 ± 8	63 ± 42
LML 137-22-137, q	12 ± 2	60 ± 1	2.5 ± 0.1	51 ± 1	16 ± 12	23 ± 12	6 ± 4
LML 137-22-137, mc	34 ± 2	155 ± 28	2.6 ± 0.2	60 ± 2	17 ± 13	45 ± 2	8 ± 6
LML 137-22-137, cc	39 ± 2	157 ± 7	2.6 ± 0.1	57 ± 2	9 ± 3	39 ± 6	4 ± 1
HIPS		91 ± 4	1.54 ± 0.04	16 ± 1	38 ± 5	19 ± 1	6 ± 1
PS[d]	[f]	99 ± 3	2.9 ± 0.3	[e]	1.4 ± 0.1	37 ± 6	0.28 ± 0.07

[a]Error bars denote 95% confidence intervals calculated using a student's t test statistic. [b]Crystallinity was measured using sections of the same films used to prepare tensile specimens. Three replicates were performed. [c]HDT was measured using a small piece of film twice as thick as the tensile specimens and subjected to an identical thermal history. Three replicates were performed. [d]The reported precision for Young's modulus is extended to show the finite confidence interval width where necessary. [e]Only four PS samples had acceptable breaks due to cracks outside the gauge length that occurred during sample preparation due to the high fragility and brittleness. [f]PS underwent brittle fracture, exhibiting no yield point.

S42).[102] Curiously, for the 22-kg mol^{-1} midblock series, shorter end-blocks crystallize more slowly at high T_c. We speculate that while PγMCL domain surfaces may speed primary nucleation, secondary nucleation is slower for shorter end-blocks due to the comparatively greater influence of interfacial mobility restrictions (see Discussion S43).

Figure 5b displays the crystallinities and HDTs measured for L78 and the 22-kg mol^{-1} midblock library resulting from (1) rapid quenching from the melt, (2) melt crystallization at 100 °C for 5 min, and (3) cold crystallization at 100 °C for 5 min. After rapid quenching, all polymers display low crystallinities and HDTs limited by $T_{g,PLLA}$. After the melt and cold crystallization routines, the LML triblocks exhibit crystallinities ranging from 39 and 55% and HDTs between 144 and 157 °C, comparable to L78. In agreement with the HDT data, the crystallization routines eliminate the storage modulus valley between 60 and 100 °C in DMTA (e.g., in Figure 4d), with a rubbery plateau extending from $T_{g,PLLA}$ to T_m and modulus values directly correlated to f_{PLLA} (Figure S44a,b). The magnitude and area of the loss tangent peaks at $T_{g,PLLA}$ are reduced, reflecting the crystallization of mobile amorphous chains and the attendant generation of a neighboring rigid amorphous fraction (Figure S44c,d).

Mechanical Properties and Deformed Microstructure. Figure 6 displays representative stress−strain curves for L78 and the 22-kg mol^{-1} midblock LML library for specimens created using the three thermal histories described above: rapid quenching, melt crystallization, and cold crystallization. The initial crystallinity, HDT, and tensile properties of each specimen type are listed in Table 2. The corresponding data for the 11-kg mol^{-1} LML library are provided in Figure S46 and Table S47. The full sets of stress−strain curves for all materials are given in Figures S48−S51. Samples were initially aged for 12 days at room temperature prior to testing to allow for the complete densification and native embrittlement of the PLLA matrix.[103]

Young's moduli of the materials range from 1.0 to 3.1 GPa, with modulus correlated to the PLLA content, indicating coupled PγMCL and PLLA deformation in the elastic regime. Interestingly, the modulus only increases with crystallinity for LML 63-11-63, whereas it is insensitive to crystallinity for LMLs 24-11-24, 37-22-37, and 137-22-137, and it decreases with crystallinity for the two lowest-f_{PLLA} materials, LML 18-

https://doi.org/10.1021/acs.macromol.3c02580
Macromolecules 2024, 57, 2818−2834

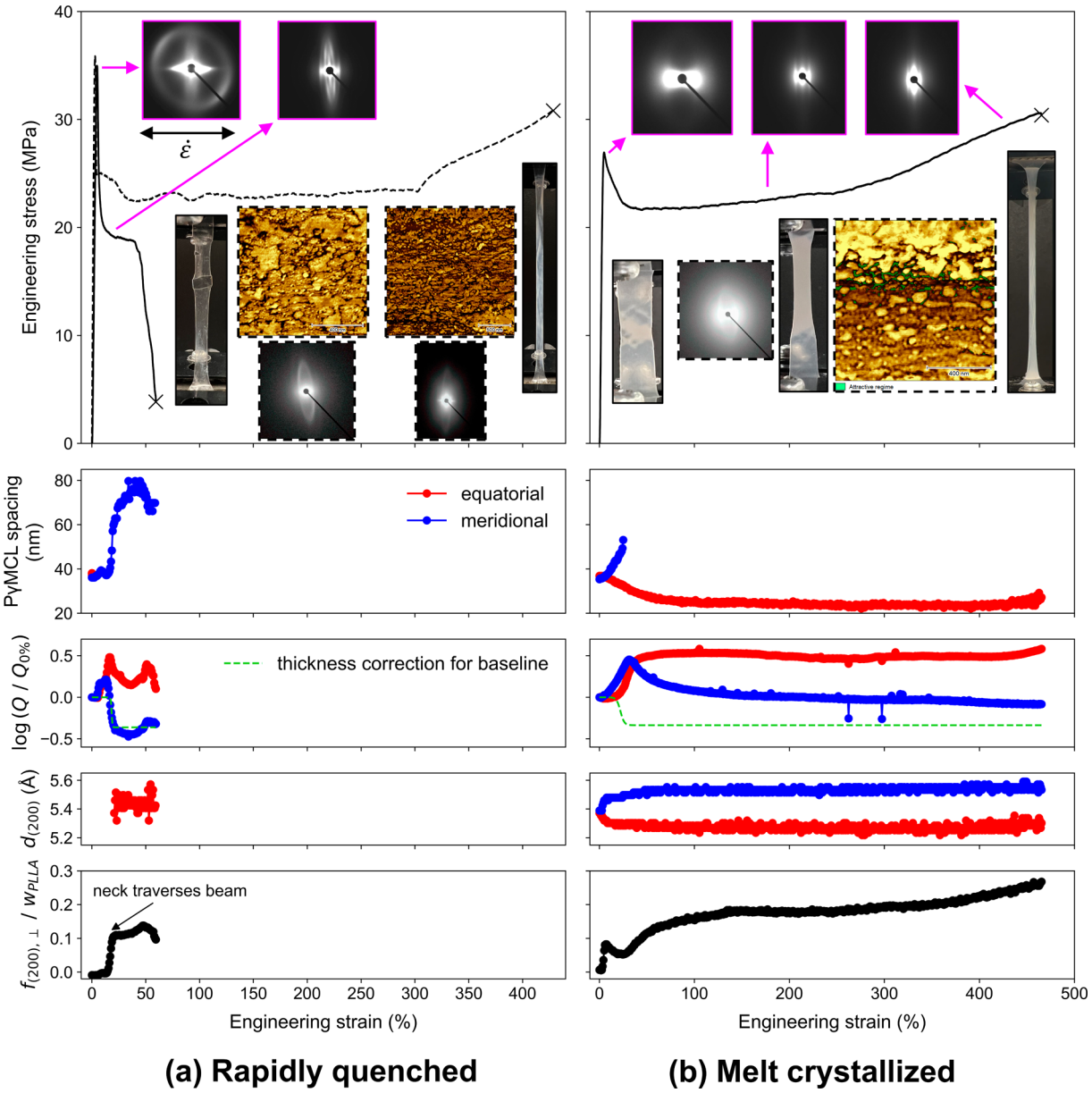

Figure 7. *In situ* tensile X-ray scattering results for LML 37-22-37 in (a) rapidly quenched and (b) melt crystallized states. The dashed line in the stress−strain panel of panel a shows representative mechanical properties for LML 37-22-37 in the rapidly quenched state. *Ex situ* X-ray scattering and AFM phase images are, respectively, reproduced from Figures S56 and S37a. The drawing direction for all X-ray and AFM images is horizontal. *In situ* images are framed with solid magenta lines, and *ex situ* images are framed with dashed black lines. The dashed green line in the invariant plots shows the expected change in the invariant due to thickness changes based on average sample thicknesses measured before and after necking.

22-18 and LML 11-11-11. This decrease of modulus with crystallinity contrasts with the intuition that crystallization increases modulus in semicrystalline polymers, including PLLA.[104] The intercalation of rubbery domains between crystal lamellae may have positioned PγMCL interfaces to reduce the local T_g of PLLA chains that would otherwise comprise the rigid amorphous fraction at the lamellar fold surfaces.[93] Because the rigid amorphous fraction has a stiffness contribution similar to that of crystalline domains, global rubbery-crystalline impingement as occurs in the low-f_{PLLA} materials could reduce the effective rigid amorphous fraction even as crystallinity increases, decreasing modulus.[105,106] With less PγMCL-crystal interface, the effect would be more subtle, hence the insensitivity observed in the higher-f_{PLLA} materials. Along with Young's modulus, the yield stress is also correlated to f_{PLLA}, suggesting that PγMCL domains participate in the onset of plastic deformation, potentially through cavitation or stretching.[107,108]

L78 exhibits predictably low ductility, first yielding and then fracturing at 3−4% strain, regardless of crystallinity. While LML 137-22-137 retains an attractively high modulus of 2.5−2.6 GPa, most samples fractured at low strains after yielding. In the quenched state, the few ductile samples showed a double-yield, craze-then-neck process consistent with previous reports of intermediately aged, atactic PLA graft block polymers with f_{PLA} = 0.9 (Figure S49g, Movie S1).[78,109] The few ductile, highly crystalline LML 137-22-137 specimens displayed only a single yield associated with shear band coalescence and necking (Figure S49h,i, Movie S2). Evidently, for LMLs with $f_{PLLA} \geq 0.9$, the PγMCL loading does not trigger sufficient

https://doi.org/10.1021/acs.macromol.3c02580
Macromolecules 2024, 57, 2818−2834

crazing (low X_c) or shear yielding (high X_c) for meaningful and reproducible ductility improvement.

In contrast, the LMLs with lower f_{PLLA} values are much more ductile regardless of their initial crystallinities. LMLs 18-22-18 and 37-22-37, respectively, achieve strains at break of 577 and 297% after rapid quenching, resulting in toughness values that are 47 and 35 times higher than rapidly quenched L78. The materials yield by necking, and the stress plateaus as the neck propagates throughout the gauge region. Once the neck has filled the gauge length, strain-whitening emerges in the center of the gauge length and propagates outward, concurrent with the onset of a strain-hardening regime indicated by the upturn of the stress−strain data (Figure S49a,d). The highly crystalline LML 18-22-18 and 37-22-37 specimens exhibit similar toughness and improved ultimate stress, owing to more pronounced strain hardening. However, crystallization reduces the yield stress, signaling that matrix crystals facilitate shear yielding. LML 18-22-18 clearly demonstrates this effect; discrete necks emerge in the rapidly quenched specimen (Figure S59a image inset), while the gauge region of the cold crystallized specimen flows uniformly (Movie S3). Finally, for technological context, we note that LML 37-22-37 showed a higher Young's modulus, yield strength, ultimate stress, and ultimate strain than high-impact polystyrene (HIPS), exceeding its toughness by a factor of 10 to 15 across crystallinity states. Moreover, the HDT of highly crystalline LML 37-22-37 is more than 50 °C greater than that of HIPS.

We also tested melt crystallized LML 37-22-37 and all processing states of LML 18-22-18 after long aging periods. Representative stress−strain curves for specimens aged for several months are shown with dotted lines in Figures 6 and S50. In the rapidly quenched LML 18-22-18, aging only increases the yield stress, indicating that the yield process for the quenched materials is sensitive to the state of the free volume of amorphous PLLA chain segments. Conversely, extensive aging does not change the yield stresses of the highly crystalline materials and only slightly reduces ductility, thus rendering these block polymers relatively insensitive to aged-induced embrittlement.

In the case of the lower-f_{PLLA} materials, the yield stresses of the 11-kg mol^{-1} midblock LMLs were 10−50% higher in the rapidly quenched state, indicating a more difficult shear yielding process (Figures S48 and S49). However, after cold crystallization, the yield stresses more closely matched those of the 22-kg mol^{-1} midblock LMLs. The yielding behavior of rapidly quenched LMLs possibly implicates the PγMCL domains, as smaller rubbery particles require higher strains for cavitation in the 11-kg mol^{-1} midblock samples, and consequently, higher bulk stresses.[107] Additionally, the less well-entangled PLLA end-blocks and greater end-group concentration in the 11-kg mol^{-1} midblock matrices may have produced local strain-softening in the matrix, leading to earlier failure of the necked regions.

To investigate the mechanism responsible for LMLs' crystallinity-independent toughness, we performed *in situ* X-ray scattering during tensile testing of LMLs 37-22-37 and 18-22-18 in both rapidly quenched and melt crystallized states. Figure 7 displays the results for LML 37-22-37, and the contributing 1D patterns are shown in Figures S52−S55. By analyzing azimuthal slices of the 2D patterns oriented parallel and perpendicular to the draw direction, we extracted the PγMCL domain spacing, the change in the relative invariant, and the spacing of the (200) crystallographic planes in the PLLA α/α'-form unit cell along both the equatorial and meridional axes. We also extracted the fraction of matrix chains oriented in the draw direction, $f_{(200),\perp}/w_{PLLA}$, as detailed in the Supporting Information. Unfortunately, the rapidly quenched LML 37-22-37 specimen chosen for *in situ* analysis was not representatively ductile, presumably due to a sample defect from film pressing, so we have supplemented the discussion with a representative stress−strain curve (dashed line in Figure 7a). Figure 8 summarizes our mechanistic hypotheses in cartoon schematics.

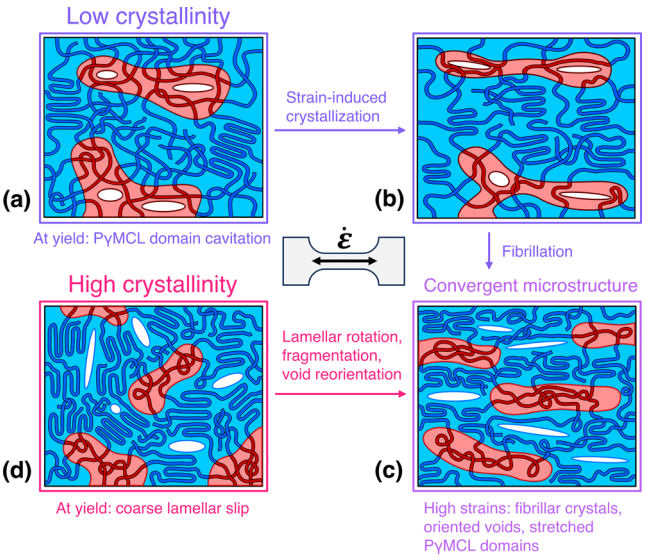

Figure 8. Cartoon schematic of tensile deformation mechanisms in low- and high-crystallinity LML triblocks.

In its rapidly quenched state (Figure 7a), LML 37-22-37 shows strong meridional streaks immediately followed by a diffuse equatorial lobe emerging in the 2D SAXS pattern as the neck traverses the X-ray beam, which suggests the presence of void-bulk interfaces resulting from cavitation, likely in the rubbery PγMCL domains (Figure 8a).[110,111] These features also signal sparse crazing, but the crazes likely play only a minor role in energy dissipation due to the rapid disappearance of the meridional streak and the persistence of only a small equatorial streak throughout the neck elongation (Movie S4). Additionally, McCutcheon et al. showed that the relative equatorial invariant monotonically increased throughout multiple crazing in PLLA,[41] whereas here it peaks at yielding but then is reduced during neck extension. The initial isotropic ring of PγMCL domain correlations distorts into an ellipse as the domain spacing is elongated along the meridional axis and contracted along the equatorial axis, showing that the PγMCL domains stretch with the PLLA matrix as it yields, also corroborated by AFM imaging. Koo et al. observed the same elliptical distortion in SAXS resulting from the stretching of rubbery poly(ethylene-*alt*-propylene) domains in a multiblock copolymer with polyethylene.[108] Necking also causes a rapid increase in the chain alignment and crystallinity (Figure 8b). The WAXS patterns in Figure S53 show consumption of the amorphous material and pronounced sharpening of the pattern at q = 1.17 Å^{-1} in the equatorial direction, corresponding to the (200)/(110) plane of the α/α'-form PLLA unit cells, and at q = 2.17 Å^{-1} in the meridional direction, corresponding to

https://doi.org/10.1021/acs.macromol.3c02580
Macromolecules 2024, 57, 2818−2834

the (1010) plane of the α-form unit cell (also visible in Movie S5). The broad WAXS peaks and heightened orientation parameters indicate a large number of small crystallites oriented with chain axes parallel to the draw direction. *Ex situ* DSC analysis of post-fracture specimens reveals that crystallinity is doubled from 20% in the pristine state to 40% in the necked state (Figure S56). The transparent neck whitens after consumption of the gauge length, and the strain-induced crystallinity enables access to the strain-hardening regime. Strain-hardening in semicrystalline polymers is generally due to the formation of fibrillar crystals connected by an oriented network of amorphous chains at large strains, and the voids between the elongated fibrils scatter light, leading to visible whitening.[112,113] Accordingly, in well-whitened gauge regions, the low-q scattering in both the equatorial and meridional directions intensifies, consistent with fibrillation and void formation, and the matrix and rubbery domains become further oriented as seen in the AFM image (Figure 7a, image inset; Figure 8c schematic). SEM imaging of fractured gauge regions also reveals the formation of interconnected fibrillated structures during neck elongation (Figure S57).

Melt-crystallized LML 37-22-37 undergoes a different failure mechanism (Figure 7b). We summarize our hypotheses here and direct the reader to Discussion S58 for a more detailed explanation of the X-ray features. A two-stage yielding process is observed concurrent with an intense "butterfly" SAXS pattern that contracts to a "two-lobe" pattern with short equatorial streaks. The meridional invariant initially peaks but is overtaken by the equatorial invariant as the stress plateaus. Together, the "butterfly" pattern and invariant crossover suggest that in the first stress drop, draw-perpendicular voids emerging in meridional spherulite regions (draw-perpendicular chain axes) from coarse lamellar slip reorient to become draw-parallel.[113−117] PγMCL domain cavitation is unlikely due to the systematically lower yield stresses resulting from crystallization and the lack of sharp meridional SAXS streaks. Instead, stress concentration resulting from discrete PγMCL domains may facilitate coarse slip of meridional lamellae at lower stresses than those required for catastrophic PLLA chain pullout during the first yield stage. The second yield stage likely involves (1) rotation and fragmentation of the slipped meridional crystal lamellae and (2) lamellar fragmentation in equatorial spherulite regions, with PγMCL domains again assisting (Figure 8d). The orientation parameter's early peak, valley, and subsequent plateau substantiate this progression. Initial fragmentation of lamellae in the meridional spherulite regions leads to an increase in orientation, followed by fragmentation in equatorial spherulite regions, reducing orientation. During neck extension, the orientation further increases from the reorganization of the original lamellae into small crystallites with draw-parallel chain axes (WAXS, Figure S55) connected by an aligned amorphous network. In the strain-hardening regime, the equatorial SAXS streaks intensify and extend outward, signaling fibrillation of the oriented amorphous chains, supported by microscopy (Figure 7b AFM image inset, Figure S57 SEM images). Taken together, these features signify the lamellar-to-fibrillar transition typical of ductile semicrystalline polymers,[113,118−121] the first demonstrated for a PLLA-rich thermoplastic drawn at room temperature to the best of our knowledge.

LML composition influences the tensile failure mechanism. The analogous *in situ* data set for LML 18-22-18 (f_{PLLA} = 0.61) and its contributing patterns are shown in Figures S59−S63, and *ex situ* X-ray analysis is shown in Figure S64. Similarly to LML 37-22-37, the neck regions of LML 18-22-18 feature stretched PγMCL domains and considerable strain-induced crystallization. However, SAXS showed much weaker signatures of PγMCL domain cavitation in the rapidly quenched material, suggesting that the abundance of PγMCL reduced the shear stress below the critical cavitation stress. For the highly crystalline specimens, we observed much less PLLA chain orientation than in LML 37-22-37, consistent with less matrix alignment and fibrillation detected in microscopy (Figures S59 inset and S65). LML 137-22-137 (f_{PLLA} = 0.92) has starkly contrasting behavior, as evidenced from *ex situ* X-ray analysis (Figure S66). Rapidly quenched specimens follow a craze-then-yield progression, while highly crystalline materials exhibit lamellar reconfigurations and moderate fibrillation. AFM reveals that LML 137-22-137 necked regions have the most pronounced matrix orientation out of all materials (Figure S38a). However, WAXS and SEM (Figure S67) suggest a less complete lamellar-to-fibrillar transition than that observed in LML 37-22-37. These compositional differences are discussed in more detail in the Supporting Information.

Finally, we investigated LML impact toughness. Encouraged by its combination of Young's modulus, ductility, and strength, we scaled up the synthesis of LML 37-22-37, producing a similar LML 43-22-43 sample. Noting that higher matrix crystallinity is generally associated with higher impact toughness in neat PLLA and in rubber-toughened PLLA blends with small (<0.3 μm) rubber particles, we tested melt crystallized LML 43-22-43.[122,123] Figure S68a compares the toughness measured for LML 43-22-43 and the HIPS control. LML 43-22-43 exhibits a notched impact toughness of 4.5 ± 0.2 kJ m^{-2}, approximately half that of HIPS (8.9 ± 0.1 kJ m^{-2}) and a factor of 3 greater than typical values of 1−2 kJ m^{-2} reported for neat PLLA.[122,124] The impact-fractured surface of LML 43-22-43 was imaged using SEM to investigate the origin of the relatively low toughness (Figure 68b). Platelet-like structures lined with fibrous anchors indicate local matrix yielding. However, the massive shear yielding characteristic of ultra-tough, highly crystalline PLLA blends is absent, suggesting that the PγMCL midblock domains fail to trigger meaningful yielding on the millisecond time scales of impact testing. This may be due to their small (~20 nm) size as compared to micrometer-sized particles in toughened blends, which can more easily cavitate and initiate crazing and shear yielding. Evidently, effective impact toughening of crystalline PLLA requires matrix-additive interactions on length scales larger than those of crystal lamellar long periods.

■ CONCLUSIONS

We evaluated neat PLLA-*b*-PγMCL-*b*-PLLA triblock polymers as tough, thermally resilient, renewable plastics. During chain extension of telechelic PγMCL macroinitiators, homopolymer PLLA and LM diblock chains were produced alongside the target LML triblocks due to adventitious impurities. Two complementary and generalizable schemes were developed and used to quantify impurity species. The LML melt microstructure was highly sensitive to molar mass and impurity content. Low molar masses and longer annealing times were required for ordered self-assembly, while the high-molar mass LML materials exhibited disordered morphologies. Microphase separation was preserved throughout crystallization, producing PLLA crystal lamellae intercalated with rubbery PγMCL domains. The LMLs crystallized as quickly as a PLLA

https://doi.org/10.1021/acs.macromol.3c02580
Macromolecules 2024, 57, 2818−2834

homopolymer control, showing that the triblock architecture is amenable to typical PLLA processing. In tensile testing, the LML triblocks exhibited toughness improvements by factors of three to nearly 100 while retaining Young's moduli between 1.0 and 2.6 GPa depending on the PLLA volume fraction. Remarkably, the toughness improvements were independent of matrix crystallinity. Melt and cold crystallized materials with PLLA volume fractions of 60 and 75% showed crystallinities ranging from 46 to 54%, HDTs ranging from 144 to 152 °C, and tensile toughness values ranging from 63 to 113 MJ m^{-3}. These materials also demonstrated considerable aging resistance, with improved ductility retained over months of aging.

In situ X-ray scattering during tensile testing illuminated a convergent microstructure across different sample crystallinities at high strains. Low-crystallinity LMLs underwent PγMCL domain cavitation and strain-induced crystallization, while high-crystallinity LMLs' PγMCL domains facilitated crystal lamellar slip and fragmentation, enabling both types of samples to fibrillate and strain-harden. This marks the first room temperature observation of the "lamellar-to-fibrillar" transition of ductile semicrystalline polymers in a PLLA-based thermoplastic. The LML architecture only slightly improved upon PLLA's impact toughness, suggesting that the energy dissipation length scales of neat PLLA block polymers are too small to trigger massive matrix yielding during impact fracture. This study extols the technical advantages of the neat block polymer approach to PLLA upgrading, prompting further optimization of the molecular architecture and crystallization kinetics. Additionally, the impurity quantification tools developed here will enable more accurate compositional descriptions of materials in the PLLA block polymer space, furnishing structure–property insights that are more rigorously informed by impurity content.

■ ASSOCIATED CONTENT

Data Availability Statement

All primary data files are available free of charge at 10.13020/nppq-1z11.

Supporting Information

The Supporting Information is available free of charge at https://pubs.acs.org/doi/10.1021/acs.macromol.3c02580.

Materials and methods, synthetic protocols, sample preparation and characterization methods, and impurity quantification schemes; NMR spectra, tabulated LML compositions, X-ray scattering patterns (variable-temperature, in situ and ex situ tensile); AFM images, TGA traces, DMTA traces and HDT traces; and tensile testing traces, SEM images, Izod impact toughness data, and associated supplementary discussion (PDF)

LML 137-22-137, quenched: double-yield, craze-then-neck process (MOV)

LML 137-22-137, cold crystallized: single yield, shear band coalescence and necking (MOV)

LML 18-22-18, cold crystallized: gauge region flows uniformly (MOV)

LML 37-22-37, quenched, *in situ* SAXS (AVI)

LML 37-22-37, quenched, *in situ* WAXS (AVI)

LML 37-22-37, melt crystallized, *in situ* SAXS, linearly scaled pixel intensity (AVI)

LML 37-22-37, melt crystallized, *in situ* SAXS, logarithmically scaled pixel intensity (AVI)

■ AUTHOR INFORMATION

Corresponding Author

Marc A. Hillmyer − *Department of Chemistry, University of Minnesota, Minneapolis, Minnesota 55455, United States;* orcid.org/0000-0001-8255-3853; Email: hillmyer@umn.edu

Authors

Daniel M. Krajovic − *Department of Chemical Engineering and Materials Science, University of Minnesota, Minneapolis, Minnesota 55455, United States;* orcid.org/0000-0001-5311-1941

Greg Haugstad − *Characterization Facility, University of Minnesota, Minneapolis, Minnesota 55455, United States*

Complete contact information is available at: https://pubs.acs.org/10.1021/acs.macromol.3c02580

Author Contributions

D.M.K. collected and analyzed all data and wrote the manuscript. G.H. oversaw early AFM experiments and provided significant, consistent support in identifying and mitigating bistability artifacts in AC mode. M.A.H. supervised research and secured funding for reagent and equipment purchases as well as instrument usage.

Notes

The authors declare no competing financial interest.

■ ACKNOWLEDGMENTS

We would like to acknowledge Derek Batiste, Stephanie Liffland, Claire Dingwell, Yoon-Jung Jang, Marianne Meyersohn, Satu Häkkinen, Shuang Liang, Mara Kuenen, and Matthew Larson for many helpful discussions and support with manuscript revision. We thank NatureWorks, LLC. for generously providing lactide used in these studies. SAXS experiments were performed at the DuPont-Northwestern-Dow Collaborative Access Team (DND-CAT) located at Sector 5 of the Advanced Photon Source (APS) at Argonne National Laboratory. APS is a U.S. Department of Energy (DOE) Office of Science user facility operated for the U.S. DOE Office of Science by the Argonne National Laboratory under contract no. DE-AC02- 06CH1135. DND-CAT is supported by Northwestern University, E.I. DuPont de Nemours & Co., and Dow Chemical Company. Reagent and equipment purchases and instrumental usage were funded by the Minnesota Corn Research and Promotion Council (Project 6073-22DD). D.M.K. acknowledges funding from a University of Minnesota College of Science and Engineering Fellowship and a National Science Foundation (NSF) Graduate Research Fellowship (grant no. 2237827). Any opinions, findings, conclusions, or recommendations expressed in this material are those of the authors and do not necessarily reflect the views of the NSF. G.H. acknowledges financial support from the University of Minnesota Industrial Partnership for Research in Interfacial and Materials Engineering (IPRIME) program. Parts of this research were carried out at the Characterization Facility, University of Minnesota, which receives partial support from the NSF through the MRSEC (Award Number DMR-2011401) and the NNCI (Award Number ECCS-2025124) programs.

REFERENCES

(1) Andrady, A. L.; Neal, M. A. Applications and societal benefits of plastics. *Philos. T R Soc. B* **2009**, *364* (1526), 1977−1984.
(2) Geyer, R.; Jambeck, J. R.; Law, K. L. Production, use, and fate of all plastics ever made. *Sci. Adv.* **2017**, *3* (7), No. e1700782.
(3) *The New Plastics Economy: Rethinking the future of plastics*; Ellen MacArthur Foundation and McKinsey & Company: U.K., 2016.
(4) *Breaking the Plastic Wave: A Comprehensive Assessment of Pathways Toward Stopping Ocean Plastic Pollution*; The Pew Charitable Trusts, SYSTEMIQ, 2020.
(5) Boelee, E.; Geerling, G.; van der Zaan, B.; Blauw, A.; Vethaak, A. D. Water and health: From environmental pressures to integrated responses. *Acta Trop* **2019**, *193*, 217−226.
(6) Raynaud, J. *Valuing Plastic: The Business Case for Measuring, Managing and Disclosing Plastic Use in the Consumer Goods Industry*; United Nations Environment Programme, 2014.
(7) Rochman, C. M.; Browne, M. A.; Underwood, A. J.; van Franeker, J. A.; Hompson, R. C. T.; Amaral-Zettler, L. A. The ecological impacts of marine debris: unraveling the demonstrated evidence from what is perceived. *Ecology* **2016**, *97* (2), 302−312.
(8) *The Real Truth About the U.S. Plastics Recycling Rate*; Beyond Plastics at Bennington College: Bennington, VT, 2022.
(9) *Circular Claims Fall Flat Again*; Greenpeace, Inc.: Washington D.C., 2022.
(10) Auras, R.; Harte, B.; Selke, S. An overview of polylactides as packaging materials. *Macromol. Biosci* **2004**, *4* (9), 835−864.
(11) Jandas, P. J.; Prabakaran, K.; Mohanty, S.; Nayak, S. K. Evaluation of biodegradability of disposable product prepared from poly (lactic acid) under accelerated conditions. *Polym. Degrad. Stab.* **2019**, *164*, 46−54.
(12) Muniyasamy, S.; Ofosu, O.; John, M. J.; Anandjiwala, R. D. Mineralization of Poly(lactic acid) (PLA), Poly(3-hydroxybutyrate-co-valerate) (PHBV) and PLA/PHBV Blend in Compost and Soil Environments. *J. Renew Mater.* **2016**, *4* (2), 133−145.
(13) Farah, S.; Anderson, D. G.; Langer, R. Physical and mechanical properties of PLA, and their functions in widespread applications - A comprehensive review. *Adv. Drug Deliver Rev.* **2016**, *107*, 367−392.
(14) *Bioplastics Market Development Update 2022*; European Bioplastics: Berlin, Germany, 2022.
(15) Zhao, X. P.; Hu, H.; Wang, X.; Yu, X. L.; Zhou, W. Y.; Peng, S. X. Super tough poly(lactic acid) blends: a comprehensive review. *Rsc Adv.* **2020**, *10* (22), 13316−13368.
(16) Nofar, M.; Sacligil, D.; Carreau, P. J.; Kamal, M. R.; Heuzey, M. C. Poly (lactic acid) blends: Processing, properties and applications. *Int. J. Biol. Macromol.* **2019**, *125*, 307−360.
(17) Gu, Z. H.; Zhang, J. G.; Cao, W.; Liu, X.; Wang, J. S.; Zhang, X. M.; Chen, W. X.; Bao, J. N. Extraordinary toughness and heat resistance enhancement of biodegradable PLA/PBS blends through the formation of a small amount of interface-localized stereocomplex crystallites during melt blending. *Polymer* **2022**, *262*, No. 125454.
(18) Kilic, N. T.; Can, B. N.; Kodal, M.; Ozkoc, G. Compatibilization of PLA/PBAT blends by using Epoxy-POSS. *J. Appl. Polym. Sci.* **2019**, *136* (12), 47217.
(19) Liu, H. Z.; Chen, N.; Peng, C. Q.; Zhang, S.; Liu, T.; Song, P. A.; Zhong, G. L.; Liu, H. Diisocyanate-Induced Dynamic Vulcanization of Difunctional Fatty Acids toward Mechanically Robust PLA Blends with Enhanced Luminescence Emission. *Macromolecules* **2022**, *55* (17), 7695−7710.
(20) Wang, Z.; Zhang, K. L.; Wang, H. T.; Wu, X. Y.; Wang, H. Y.; Weng, C. L.; Li, Y. J.; Liu, S. Q.; Yang, J. T. Strengthening Interfacial Adhesion and Foamability of Immiscible Polymer Blends via Rationally Designed Reactive Macromolecular Compatibilizers. *Acs Appl. Mater. Inter* **2022**, *14* (40), 45832−45843.
(21) Wen, J. X.; Yi, L. X.; Su, J. J.; Han, J. In-situ reactive compatiblization modified poly(L-lactic acid) and poly (butylene adipate-co-terephthalate) blends with improved toughening and thermal characteristics. *Int. J. Biol. Macromol.* **2023**, *231*, No. 123419.
(22) Yang, H. R.; Jia, G.; Wu, H.; Ye, C. C.; Yuan, K.; Liu, S. L.; Zhou, L. M.; Xu, H.; Gao, L. J.; Cui, J.; Fang, S. M. Design of fully biodegradable super-toughened PLA/PBAT blends with asymmetric composition via reactive compatibilization and controlling morphology. *Mater. Lett.* **2022**, *329*, No. 133067.
(23) Yang, X.; Wei, F.; Wang, Z.; Li, G.; Yang, S.; Feng, J. High-reactive silica nanosheets as compatibilizers for immiscible PLLA/PBAT polymer blends. *Compos. Sci. Technol.* **2023**, *236*, No. 109979.
(24) Zhang, B.; Sun, B.; Bian, X. C.; Li, G.; Chen, X. S. High Melt Strength and High Toughness PLLA/PBS Blends by Copolymerization and in Situ Reactive Compatibilization. *Ind. Eng. Chem. Res.* **2017**, *56* (1), 52−62.
(25) Anderson, K. S.; Hillmyer, M. A. The influence of block copolymer microstructure on the toughness of compatibilized polylactide/polyethylene blends. *Polymer* **2004**, *45* (26), 8809−8823.
(26) Anderson, K. S.; Lim, S. H.; Hillmyer, M. A. Toughening of polylactide by melt blending with linear low-density polyethylene. *J. Appl. Polym. Sci.* **2003**, *89* (14), 3757−3768.
(27) Supthanyakul, R.; Kaabbuathong, N.; Chirachanchai, S. Poly(L-lactide-b-butylene succinate-b-L-lactide) triblock copolymer: A multifunctional additive for PLA/PBS blend with a key performance on film clarity. *Polym. Degrad. Stab.* **2017**, *142*, 160−168.
(28) Chen, J. L.; Rong, C. Y.; Lin, T. T.; Chen, Y. H.; Wu, J. L.; You, J. C.; Wang, H. T.; Li, Y. J. Stable Co-Continuous PLA/PBAT Blends Compatibilized by Interfacial Stereocomplex Crystallites: Toward Full Biodegradable Polymer Blends with Simultaneously Enhanced Mechanical Properties and Crystallization Rates. *Macromolecules* **2021**, *54* (6), 2852−2861.
(29) Chen, X. J.; Li, C. X.; Ding, Y. L.; Li, Y.; Li, J. S.; Sun, L. M.; Wei, J.; Wei, X. H.; Wang, H.; Zhang, K. Y.; Pan, L.; Li, Y. S. Fully Bio-Based and Supertough PLA Blends via a Novel Interlocking Strategy Combining Strong Dipolar Interactions and Stereocomplexation. *Macromolecules* **2022**, *55* (13), 5864−5878.
(30) Chen, Y. H.; Wu, J. L.; Qu, Y. D.; Ling, X. Y.; Wang, H. T.; Li, Y. J. Immiscible Polymer Blends Compatibilized through Noncovalent Forces: Construction of a ?Quasi-Block/Graft Copolymer? by Interfacial Stereocomplex Crystallites. *Acs Appl. Polym. Mater.* **2022**, *4* (12), 9378−9387.
(31) Fang, M. G.; Luo, C. Y.; Guo, X. Y.; Sun, J. X.; Chen, M. Y.; Chen, W. X. The Effect of Cellulose Nanocrystals and Acetylated Nanocellulose on the Crystallization Kinetics and Thermal Stability of Polylactic Acid. *Polym. Sci. Ser. A* **2022**, *64* (6), 802−817.
(32) Genovese, M. E.; Puccinelli, L.; Mancini, G.; Carzino, R.; Goldoni, L.; Castelvetro, V.; Athanassiou, A. Rapid Solvent-Free Microcrystalline Cellulose Melt Functionalization with L-Lactide for the Fabrication of Green Poly(lactic acid) Biocomposites. *ACS SUSTAINABLE CHEMISTRY & ENGINEERING* **2022**, *10* (29), 9401−9410.
(33) Wan, Z. W.; Li, M. L.; Zhuang, Y. Z.; Tong, Z. Z. Effect of electrospun stereocomplex PLA fibers and modified cellulose nanocrystals on crystallization of poly(L-lactic acid). *J. Appl. Polym. Sci.* **2023**, *140* (19), No. e53839.
(34) Macke, N.; Hemmingsen, C. M.; Rowan, S. J. The effect of polymer grafting on the mechanical properties of PEG-grafted cellulose nanocrystals in poly(lactic acid). *J. Polym. Sci.* **2022**, *60* (24), 3318−3330.
(35) Kim, S. J.; Eom, T. G.; Kang, S. K.; Seo, M.; Jeong, Y. G. Sustainable and high-performance composites based on glycidyl methacrylate-grafted poly(lactic acid) and cellulose nanofibrils. *J. Appl. Polym. Sci.* **2023**, *140* (15), No. e53732.
(36) Kowalczyk, M.; Pluta, M.; Piorkowska, E.; Krasnikova, N. Plasticization of polylactide with block copolymers of ethylene glycol and propylene glycol. *J. Appl. Polym. Sci.* **2012**, *125* (6), 4292−4301.
(37) Li, T. Q.; Zhang, J. Y.; Schneiderman, D. K.; Francis, L. F.; Bates, F. S. Toughening Glassy Poly(lactide) with Block Copolymer Micelles. *ACS Macro Lett.* **2016**, *5* (3), 359−364.
(38) McCutcheon, C. J.; Zhao, B. R.; Jin, K. L.; Bates, F. S.; Ellison, C. J. Crazing Mechanism and Physical Aging of Poly(lactide) Toughened with Poly(ethylene oxide)-block-poly(butylene oxide) Diblock Copolymers. *Macromolecules* **2020**, *53* (22), 10163−10178.

https://doi.org/10.1021/acs.macromol.3c02580
Macromolecules 2024, 57, 2818−2834

(39) Zhao, B. R.; McCutcheon, C. J.; Jin, K. L.; Lyadov, I.; Zervoudakis, A. J.; Bates, F. S.; Ellison, C. J. Enhanced Mechanical Properties of Uniaxially Stretched Polylactide/Poly(ethylene oxide)-b-Poly(butylene oxide) Blend Films. *Acs Appl. Polym. Mater.* **2022**, *4* (11), 8705−8714.
(40) Gu, L. L.; Nessim, E. E.; Li, T. Q.; Macosko, C. W. Toughening poly(lactic acid) with poly(ethylene oxide)-poly(propylene oxide)-poly(ethylene oxide) triblock copolymers. *Polymer* **2018**, *156*, 261−269.
(41) McCutcheon, C. J.; Zhao, B.; Ellison, C. J.; Bates, F. S. Crazing and Toughness in Diblock Copolymer-Modified Semicrystalline Poly(L-lactide). *Macromolecules* **2021**, *54* (23), 11154−11169.
(42) Lin, H.; Chen, Y.; Gao, X. R.; Xu, L.; Lei, J.; Zhong, G. J.; Li, Z. M. Transparent, Heat-Resistant, Ductile, and Self-Reinforced Polylactide through Simultaneous Formation of Nanocrystals and an Oriented Amorphous Phase. *Macromolecules* **2023**, *56* (6), 2454−2464.
(43) Razavi, M.; Wang, S. Q. Why Is Crystalline Poly(lactic acid) Brittle at Room Temperature? *Macromolecules* **2019**, *52* (14), 5429−5441.
(44) Brosset, M.; Herrmann, L.; Falher, T.; Brinkmann, M. Preparation of oriented poly(lactic acid) thin films by a combination of high temperature rubbing and thermal annealing: Impact of annealing parameters on structure, polymorphism and morphology. *J. Polym. Sci.* **2023**, *61* (9), 829−841.
(45) Liu, P. F.; Zhang, Q.; Wu, H.; Guo, S. Y.; Qiu, J. H. In Situ Formation of Soft-Rigid Hybrid Fibers Decorated by Sparse Lamellae of PLLA: Achieving Ductile and Heat-Resistant Materials with High Strength. *Macromolecules* **2023**, *56* (2), 634−646.
(46) Huang, W. J.; Zhu, N.; Liu, Y. H.; Wang, J.; Zhong, J.; Sun, Q.; Sun, T.; Hu, X.; Fang, Z.; Guo, K. A novel microfluidic enzyme-organocatalysis combination strategy for ringopening copolymerizations of lactone, lactide and cyclic carbonate. *Chem. Eng. J.* **2019**, *356*, 592−597.
(47) Ji, C. L.; Jie, S. Y.; Li, B. G. Ring-opening Copolymerization of L-Lactide and delta-Valerolactone Catalyzed by Benzoxazolyl Urea Catalyst/MTBD. *Acta Polym. Sin.* **2022**, *53* (5), 488−496.
(48) Wang, X.; Liu, J. Q.; Xu, S. Q.; Xu, J. X.; Pan, X. F.; Liu, J. J.; Cui, S. D.; Li, Z. J.; Guo, K. Traceless switch organocatalysis enables multiblock ring-opening copolymerizations of lactones, carbonates, and lactides: by a one plus one approach in one pot. *Polym. Chem.* **2016**, *7* (41), 6297−6308.
(49) Zhu, Y. J.; Gao, L. Y.; Li, Z. J.; Liu, B.; Zhang, Z. H.; Tong, H. Y.; Qu, Y. Y.; Quan, Y. S.; Zou, X.; Guo, K. Merging of cationic RAFT and radical RAFT polymerizations with ring-opening polymerizations for the synthesis of asymmetric ABCD type tetrablock copolymers in one pot. *POLYMER CHEMISTRY* **2021**, *12* (34), 4974−4985.
(50) Zhu, Y. J.; Hu, Y. Z.; Li, Z. J.; Liu, B.; Qu, Y. Y.; Zhang, Z. H.; Guo, T. F.; Li, Y. Q.; Gao, L. Y.; Guo, K. A genuine H-bond donor and Lewis base amine cocatalyst in ring-opening polymerizations. *Eur. Polym. J.* **2021**, *143*, No. 110184.
(51) Baimark, Y.; Srisuwan, Y. Thermal and mechanical properties of highly flexible poly(L-lactide)-b-poly(ethylene glycol)-b-poly(L-lactide) bioplastics: Effects of poly(ethylene glycol) block length and chain extender. *Journal of Elastomers & Plastics* **2020**, *52* (2), 142−158.
(52) *Physical Properties of Polymers Handbook*; 2 ed.; Spriner-Verlag: New York, NY, 2007; p. 1076.
(53) Lebarbe, T.; Ibarboure, E.; Gadenne, B.; Alfos, C.; Cramail, H. Fully bio-based poly(L-lactide)-b-poly(ricinoleic acid)-b-poly(L-lactide) triblock copolyesters: investigation of solid-state morphology and thermo-mechanical properties. *Polym. Chem.* **2013**, *4* (11), 3357−3369.
(54) Ogawa, R.; Hillmyer, M. A. High molar mass poly(ricinoleic acid) via entropy-driven ring-opening metathesis polymerization. *Polym. Chem.* **2021**, *12* (15), 2253−2257.
(55) Engelberg, I.; Kohn, J. Physicomechanical Properties of Degradable Polymers Used in Medical Applications - a Comparative-Study. *Biomaterials* **1991**, *12* (3), 292−304.
(56) Tsuji, H.; Ikada, Y. Stereocomplex formation between enantiomeric poly(lactic acid)s. XI. Mechanical properties and morphology of solution-cast films. *Polymer* **1999**, *40* (24), 6699−6708.
(57) Panthani, T. R.; Bates, F. S. Crystallization and Mechanical Properties of Poly(L-lactide)-Based Rubbery/Semicrystalline Multiblock Copolymers. *Macromolecules* **2015**, *48* (13), 4529−4540.
(58) Lee, I.; Panthani, T. R.; Bates, F. S. Sustainable Poly(lactide-b-butadiene) Multiblock Copolymers with Enhanced Mechanical Properties. *Macromolecules* **2013**, *46* (18), 7387−7398.
(59) Ojha, U.; Kulkarni, P.; Singh, J.; Faust, R. Syntheses, Characterization, and Properties of Multiblock Copolymers Consisting of Polyisobutylene and Poly(L-lactide) Segments. *J. Polym. Sci. Pol Chem.* **2009**, *47* (14), 3490−3505.
(60) Chen, Y. P.; Zhang, J. A.; Zhang, Y. S.; Cao, W.; Liu, X.; Bao, J. N.; Zhang, X. M.; Chen, W. X. Poly(L-lactide)-b-poly(& epsilon;-caprolactone)-b-poly(D,L-lactide) copolymers with enhanced toughness and strength by regulating crystallization and phase separation. *J. Polym. Sci.* **2023**, *61* (19), 2303−2315.
(61) Zhang, J. Y.; Li, T. Q.; Mannion, A. M.; Schneiderman, D. K.; Hillmyer, M. A.; Bates, F. S. Tough and Sustainable Graft Block Copolymer Thermoplastics. *ACS Macro Lett.* **2016**, *5* (3), 407−412.
(62) Zhang, J. Y.; Schneiderrnan, D. K.; Li, T. Q.; Hillmyer, M. A.; Bates, F. S. Design of Graft Block Polymer Thermoplastics. *Macromolecules* **2016**, *49* (23), 9108−9118.
(63) Lundberg, D. J.; Lundberg, D. J.; Hillmyer, M. A.; Dauenhauer, P. J. Techno-economic Analysis of a Chemical Process To Manufacture Methyl-epsilon-caprolactone from Cresols. *Acs Sustainable Chemistry & Engineering* **2018**, *6* (11), 15316−15324.
(64) Breteler, M. R. T.; Zhong, Z.; Dijkstra, P. J.; Palmans, A. R. A.; Peeters, J.; Feijen, J. Ring-opening polymerization of substituted ε-caprolactones with a chiral (salen) AlOiPr complex. *J. Polym. Sci., Part A: Polym. Chem.* **2007**, *45* (3), 429−436.
(65) Olsen, P.; Odelius, K.; Albertsson, A. C. Thermodynamic Presynthetic Considerations for Ring-Opening Polymerization. *Biomacromolecules* **2016**, *17* (3), 699−709.
(66) Watts, A.; Kurokawa, N.; Hillmyer, M. A. Strong, Resilient, and Sustainable Aliphatic Polyester Thermoplastic Elastomers. *Biomacromolecules* **2017**, *18* (6), 1845−1854.
(67) Batiste, D. C.; De Hoe, G. X.; Nelson, T. F.; Sodnikar, K.; McNeill, K.; Sander, M.; Hillmyer, M. A. Site-Specific Mineralization of a Polyester Hydrolysis Product in Natural Soil. *ACS Sustainable Chem. Eng.* **2022**, *10* (4), 1373−1378.
(68) De Hoe, G. X.; Zumstein, M. T.; Tiegs, B. J.; Brutman, J. P.; McNeill, K.; Sander, M.; Coates, G. W.; Hillmyer, M. A. Sustainable Polyester Elastomers from Lactones: Synthesis, Properties, and Enzymatic Hydrolyzability. *J. Am. Chem. Soc.* **2018**, *140* (3), 963−973.
(69) Self, J. L.; Sample, C. S.; Levi, A. E.; Li, K. X.; Xie, R. X.; de Alaniz, J. R.; Bates, C. M. Dynamic Bottlebrush Polymer Networks: Self-Healing in Super-Soft Materials. *J. Am. Chem. Soc.* **2020**, *142* (16), 7567−7573.
(70) Meyersohn, M. S.; Haque, F. M.; Hillmyer, M. A. Dynamic Aliphatic Polyester Elastomers Crosslinked with Aliphatic Dianhydrides. *ACS Polymers Au* **2023**, *3* (5), 365−375.
(71) Xie, R. X.; Lapkriengkri, I.; Pramanik, N. B.; Mukherjee, S.; Blankenship, J. R.; Albanese, K.; Wang, H. B.; Chabinyc, M. L.; Bates, C. M. Hydrogen-Bonding Bottlebrush Networks: Self-Healing Materials from Super-Soft to Stiff. *Macromolecules* **2022**, *55* (23), 10513−10521.
(72) Reisman, L.; Siehr, A.; Horn, J.; Batiste, D. C.; Kim, H. J.; De Hoe, G. X.; Ellison, C. J.; Shen, W.; White, E. M.; Hillmyer, M. A. Respirometry and Cell Viability Studies for Sustainable Polyesters and Their Hydrolysis Products. *Acs Sustainable Chemistry & Engineering* **2021**, *9* (7), 2736−2744.
(73) Albanese, K. R.; Blankenship, J. R.; Quah, T.; Zhang, A.; Delaney, K. T.; Fredrickson, G. H.; Bates, C. M.; Hawker, C. J. Improved Elastic Recovery from ABC Triblock Terpolymers. *Acs Polymers Au* **2023**, *3* (5), 376−382.

(74) Liffland, S.; Hillmyer, M. A. Enhanced Mechanical Properties of Aliphatic Polyester Thermoplastic Elastomers through Star Block Architectures. *Macromolecules* **2021**, *54* (20), 9327−9340.
(75) Liffland, S.; Kumler, M.; Hillmyer, M. A. High Performance Star Block Aliphatic Polyester Thermoplastic Elastomers Using PDLA-b-PLLA Stereoblock Hard Domains. *ACS Macro Lett.* **2023**, *12*, 1331−1338.
(76) Fournier, L.; Mirabal, D. M. R.; Hillmyer, M. A. Toward Sustainable Elastomers from the Grafting-Through Polymerization of Lactone-Containing Polyester Macromonomers. *Macromolecules* **2022**, *55* (3), 1003−1014.
(77) Blankenship, J. R.; Levi, A. E.; Goldfeld, D. J.; Self, J. L.; Alizadeh, N.; Chen, D. Y.; Fredrickson, G. H.; Bates, C. M. Asymmetric Miktoarm Star Polymers as Polyester Thermoplastic Elastomers. *Macromolecules* **2022**, *55* (12), 4929−4936.
(78) Haugan, I. N.; Lee, B.; Maher, M. J.; Zografos, A.; Schibur, H. J.; Jones, S. D.; Hillmyer, M. A.; Bates, F. S. Physical Aging of Polylactide-Based Graft Block Polymers. *Macromolecules* **2019**, *52* (22), 8878−8894.
(79) Batiste, D. C.; Meyersohn, M. S.; Watts, A.; Hillmyer, M. A. Efficient Polymerization of Methyl-epsilon-Caprolactone Mixtures To Access Sustainable Aliphatic Polyesters. *Macromolecules* **2020**, *53* (5), 1795−1808.
(80) Nijenhuis, A. J.; Grijpma, D. W.; Pennings, A. J. Lewis Acid-Catalyzed Polymerization of L-Lactide - Kinetics and Mechanism of the Bulk-Polymerization. *Macromolecules* **1992**, *25* (24), 6419−6424.
(81) Witzke, D. R.; Narayan, R.; Kolstad, J. J. Reversible kinetics and thermodynamics of the homopolymerization of L-lactide with 2-ethylhexanoic acid tin(II) salt. *Macromolecules* **1997**, *30* (23), 7075−7085.
(82) Kimishima, K.; Hashimoto, T.; Han, C. D. Spatial-Distribution of Added Homopolymer within the Microdomains of a Mixture Consisting of an Aba-Type Triblock Copolymer and a Homopolymer. *Macromolecules* **1995**, *28* (11), 3842−3853.
(83) Matsen, M. W.; Thompson, R. B. Equilibrium behavior of symmetric ABA triblock copolymer melts. *J. Chem. Phys.* **1999**, *111* (15), 7139−7146.
(84) Bersenev, E. A.; Nikitina, E. A.; Dashtimoghadam, E.; Sheiko, S. S.; Ivanov, D. A. Bottlebrush Elastomers with Crystallizable Side Chains: Monitoring Configuration of Polymer Backbones in the Amorphous Regions during Crystallization. *ACS Macro Lett.* **2022**, *11* (9), 1085−1090.
(85) Koo, C. M.; Wu, L. F.; Lim, L. S.; Mahanthappa, M. K.; Hillmyer, M. A.; Bates, F. S. Microstructure and mechanical properties of semicrystalline-rubbery-semicrystalline triblock copolymers. *Macromolecules* **2005**, *38* (14), 6090−6098.
(86) Loo, Y. L.; Register, R. A.; Ryan, A. J. Modes of crystallization in block copolymer microdomains: Breakout, templated, and confined. *Macromolecules* **2002**, *35* (6), 2365−2374.
(87) Yang, J. J.; Liang, Y. R.; Luo, J.; Zhao, C. Z.; Han, C. C. Multilength Scale Studies of the Confined Crystallization in Poly(L-lactide)-block-Poly(ethylene glycol) Copolymer. *Macromolecules* **2012**, *45* (10), 4254−4261.
(88) Spontak, R. J.; Patel, N. P., Phase Behaviour of Block Copolymer Blends. In *Developments in Block Copolymer Science and Technology*; John Wiley & Sons, Ltd, 2004; pp. 159−212.
(89) Lee, S.; Gillard, T. M.; Bates, F. S. Fluctuations, Order, and Disorder in Short Diblock Copolymers. *AIChE J.* **2013**, *59* (9), 3502−3513.
(90) Winey, K. I.; Thomas, E. L.; Fetters, L. J. Isothermal Morphology Diagrams for Binary Blends of Diblock Copolymer and Homopolymer. *Macromolecules* **1992**, *25* (10), 2645−2650.
(91) Cam, D.; Marucci, M. Influence of residual monomers and metals on poly (L-lactide) thermal stability. *Polymer* **1997**, *38* (8), 1879−1884.
(92) Fillon, B.; Thierry, A.; Lotz, B.; Wittmann, J. C. Efficiency Scale for Polymer Nucleating-Agents. *J. Therm. Anal.* **1994**, *42* (4), 721−731.
(93) Christie, D.; Register, R. A.; Priestley, R. D. Role of Chain Connectivity across an Interface on the Dynamics of a Nanostructured Block Copolymer. *Phys. Rev. Lett.* **2018**, *121* (24), No. 247801.
(94) Cristea, M.; Ionita, D.; Iftime, M. M. Dynamic Mechanical Analysis Investigations of PLA-Based Renewable Materials: How Are They Useful? *Materials* **2020**, *13* (22), 5302.
(95) Saeidlou, S.; Huneault, M. A.; Li, H. B.; Park, C. B. Poly(lactic acid) crystallization. *Prog. Polym. Sci.* **2012**, *37* (12), 1657−1677.
(96) Zhang, J.; Tashiro, K.; Tsuji, H.; Domb, A. J. Disorder-to-Order Phase Transition and Multiple Melting Behavior of Poly(l-lactide) Investigated by Simultaneous Measurements of WAXD and DSC. *Macromolecules* **2008**, *41* (4), 1352−1357.
(97) Zhang, J.; Duan, Y.; Sato, H.; Tsuji, H.; Noda, I.; Yan, S.; Ozaki, Y. Crystal Modifications and Thermal Behavior of Poly(l-lactic acid) Revealed by Infrared Spectroscopy. *Macromolecules* **2005**, *38* (19), 8012−8021.
(98) Di Lorenzo, M. L.; Androsch, R. Influence of alpha '-/alpha-crystal polymorphism on properties of poly(l-lactic acid). *Polym. Int.* **2019**, *68* (3), 320−334.
(99) Yasuniwa, M.; Tsubakihara, S.; Iura, K.; Ono, Y.; Dan, Y.; Takahashi, K. Crystallization behavior of poly(L-lactic acid). *Polymer* **2006**, *47* (21), 7554−7563.
(100) Pan, P.; Kai, W.; Zhu, B.; Dong, T.; Inoue, Y. Polymorphous Crystallization and Multiple Melting Behavior of Poly(l-lactide): Molecular Weight Dependence. *Macromolecules* **2007**, *40* (19), 6898−6905.
(101) Hoffman, J. D.; Weeks, J. J. X-Ray Study of Isothermal Thickening of Lamellae in Bulk Polyethylene at the Crystallization Temperature. *J. Chem. Phys.* **1965**, *42* (12), 4301−4302.
(102) Floudas, G.; Tsitsilianis, C. Crystallization Kinetics of Poly(ethylene oxide) in Poly(ethylene oxide)−Polystyrene−Poly(ethylene oxide) Triblock Copolymers. *Macromolecules* **1997**, *30* (15), 4381−4390.
(103) Pan, P. J.; Zhu, B.; Inoue, Y. Enthalpy relaxation and embrittlement of Poly(L-lactide) during physical aging. *Macromolecules* **2007**, *40* (26), 9664−9671.
(104) Jariyavidyanont, K.; Yu, Q.; Petzold, A.; Thurn-Albrecht, T.; Glüge, R.; Altenbach, H.; Androsch, R. Young's modulus of the different crystalline phases of poly (l-lactic acid). *Journal of the Mechanical Behavior of Biomedical Materials* **2023**, *137*, No. 105546.
(105) Di Lorenzo, M. L.; Righetti, M. C. The three-phase structure of isotactic poly(1-butene). *Polymer* **2008**, *49* (5), 1323−1331.
(106) Lizundia, E.; Petisco, S.; Sarasua, J. R. Phase-structure and mechanical properties of isothermally melt-and cold-crystallized poly (L-lactide). *Journal of the Mechanical Behavior of Biomedical Materials* **2013**, *17*, 242−251.
(107) Bucknall, C. B. Quantitative approaches to particle cavitation, shear yielding, and crazing in rubber-toughened polymers. *J. Polym. Sci. Pol Phys.* **2007**, *45* (12), 1399−1409.
(108) Koo, C. M.; Hillmyer, M. A.; Bates, F. S. Structure and properties of semicrystalline - Rubbery multiblock copolymers. *Macromolecules* **2006**, *39* (2), 667−677.
(109) Theryo, G.; Jing, F.; Pitet, L. M.; Hillmyer, M. A. Tough Polylactide Graft Copolymers. *Macromolecules* **2010**, *43* (18), 7394−7397.
(110) Argon, A. S.; Cohen, R. E. Crazing and toughness of block copolymers and blends; In *Crazing in Polymers*, Vol. 2; Kausch, H. H., Ed. Springer: Berlin, Heidelberg, 1990; pp. 301−351.
(111) Brown, H. R.; Kramer, E. J. Craze Microstructure from Small-Angle X-Ray-Scattering (Saxs). *J. Macromol. Sci. Phys.* **1981**, *B19* (3), 487−522.
(112) Lu, Y.; Men, Y. F. Cavitation-Induced Stress Whitening in Semi-Crystalline Polymers. *Macromol. Mater. Eng.* **2018**, *303* (11), No. 1800203.
(113) Xu, S. S.; Zhou, J.; Pan, P. J. Strain-induced multiscale structural evolutions of crystallized polymers: From fundamental studies to recent progresses. *Prog. Polym. Sci.* **2023**, *140*, No. 101676.

https://doi.org/10.1021/acs.macromol.3c02580
Macromolecules 2024, 57, 2818−2834

(114) Iqbal, O.; Guo, H.; Chen, W. Structural Origin of Double Yielding: The Critical Role of Crystallite Aggregate Heterogeneity. *Macromolecules* **2021**, *54* (18), 8381−8392.
(115) Kishimoto, M.; Mita, K.; Ogawa, H.; Takenaka, M. Effect of Submicron Structures on the Mechanical Behavior of Polyethylene. *Macromolecules* **2020**, *53* (20), 9097−9107.
(116) Li, X. H.; Schneider, K.; Kretzschmar, B.; Stamm, M. Deformation behavior of PP and PP/ZnO nanocomposites as studied by SAXS and WAXS. *Macromolecules* **2008**, *41* (12), 4371−4379.
(117) Zhang, X. Q.; Schneider, K.; Liu, G. M.; Chen, J. H.; Bruning, K.; Wang, D. J.; Stamm, M. Deformation-mediated superstructures and cavitation of poly (L-lactide): In-situ small-angle X-ray scattering study. *Polymer* **2012**, *53* (2), 648−656.
(118) Afeworki, M.; Brant, P.; Lustiger, A.; Norman, A. Solid-state C-13 NMR and synchrotron SAXS/WAXS studies of uniaxially-oriented polyethylene. *Solid State Nucl. Mag* **2015**, *72*, 27−40.
(119) Cai, J. L.; Hsiao, B. S.; Gross, R. A. Real-Time Structure Changes during Uniaxial Stretching of Poly (omega-pentadecalactone) by in Situ Synchrotron WAXD/SAXS Techniques. *Macromolecules* **2011**, *44* (10), 3874−3883.
(120) Li, Y.; Ma, G. Q.; Sun, Y.; Huang, H. D.; Pan, M. W.; Zhang, G. Q.; Zhong, G. J.; Li, Z. M. Understanding the Morphological and Structural Evolution of alpha- and gamma-Poly(vinylidene fluoride) During High Temperature Uniaxial Stretching by In Situ Synchrotron X-ray Scattering. *Ind. Eng. Chem. Res.* **2020**, *59* (41), 18567−18578.
(121) Wang, Y. T.; Jiang, Z. Y.; Fu, L. L.; Lu, Y.; Men, Y. F. Lamellar Thickness and Stretching Temperature Dependency of Cavitation in Semicrystalline Polymers. *PLoS One* **2014**, *9* (5), No. e97234.
(122) Bai, H. W.; Huang, C. M.; Xiu, H.; Gao, Y.; Zhang, Q.; Fu, Q. Toughening of poly(L-lactide) with poly(epsilon-caprolactone): Combined effects of matrix crystallization and impact modifier particle size. *Polymer* **2013**, *54* (19), 5257−5266.
(123) Zhang, Z. C.; Wan, X. Y.; Fan, B. M.; Ma, Y. H.; Yang, B. Nonisothermal Crystallization Behavior and Enhanced Heat Resistance and Impact Toughness of Poly(L-lactic acid) with Bimodal Molecular Weight Distribution. *Acs Sustainable Chemistry & Engineering* **2022**, *10* (49), 16459−16469.
(124) Wu, B. G.; Zeng, Q. T.; Niu, D. Y.; Yang, W. J.; Dong, W. F.; Chen, M. Q.; Ma, P. M. Design of Supertoughened and Heat-Resistant PLLA/Elastomer Blends by Controlling the Distribution of Stereocomplex Crystallites and the Morphology. *Macromolecules* **2019**, *52* (3), 1092−1103.

https://doi.org/10.1021/acs.macromol.3c02580
Macromolecules 2024, 57, 2818−2834